Investigation on a direct expansion multisource carbon dioxide heat pump to maximize the use of renewable energy sources

Conte, Riccardo; Tancon, Marco; Mozafarivanani, Mohammad; Zanetti, Emanuele; Azzolin, Marco; Del Col, Davide

DOI
10.1016/j.applthermaleng.2025.126533

Publication date
2025

Document Version
Final published version

Published in
Applied Thermal Engineering

Applied Thermal Engineering 274 (2025) 126533

Contents lists available at ScienceDirect

Applied Thermal Engineering

journal homepage: www.elsevier.com/locate/apthermeng

Research Paper

Investigation on a direct expansion multisource carbon dioxide heat pump to maximize the use of renewable energy sources☆

Riccardo Conte [a], Marco Tancon [a], Mohammad Mozafarivanani [a], Emanuele Zanetti [b], Marco Azzolin [a,*], Davide Del Col [a]

[a] Department of Industrial Engineering, University of Padova, Via Venezia 1, 35131 Padova, Italy
[b] Department of Process and Energy, Delft University of Technology, Leeghwaterstraat 39, 2628 CB Delft, the Netherlands

ARTICLE INFO

Keywords:
Multisource heat pump
Solar energy
Geothermal energy
Direct expansion
Simultaneous operations
Carbon dioxide

ABSTRACT

Traditional heat pump systems typically rely on a single low-temperature source, such as air, ground, or solar energy, each with intrinsic limitations. Air-source heat pumps are highly sensitive to temperature fluctuations across seasons and daily cycles, while the efficiency of solar-source heat pumps is constrained by the intermittent availability of solar radiation. Ground-source heat pumps, in contrast, deliver consistent seasonal performance but involve higher costs for the installation of borehole heat exchangers. Multisource heat pumps offer a promising technology to overcome these challenges and maximize the use of renewable energy.

This paper presents a numerical investigation of an innovative multisource heat pump using CO_2 as a low GWP refrigerant, that can exploit three different thermal sources through dedicated evaporators: air source with a finned coil heat exchanger, solar source with photovoltaic-thermal (PV-T) collectors, and ground source with a U-tube borehole heat exchanger (BHE). Two modes of operation are foreseen: solar-air mode (SA-mode) and ground-air mode (GA-mode). The novelty of this system lies in the concept of a multisource direct expansion heat pump in which the CO_2 directly vaporizes in flooded mode in the solar or ground evaporators, while the finned coil works in dry expansion mode. Differently from all other systems, the solar and ground evaporators operate simultaneously with the air evaporator. Simulations are performed to assess the performance of the multisource heat pump under varying environmental conditions: air temperature, solar irradiance, and soil temperature. The results demonstrate that while air temperature influences the performance of both SA-mode and GA-mode, each mode exhibits distinct sensitivities to the other environmental parameters. SA-mode performance is significantly affected by solar irradiance, with a 100 W/m^2 increase in irradiance corresponding to a 2.8 % enhancement in the coefficient of performance (COP). Conversely, GA-mode performance shows a notable response to soil temperature variations, where a 1 K increase in soil temperature results in a 0.9 % improvement in COP. The results compare SA-mode and GA-mode with air-source heat pump mode under varying thermal loads for space heating (SH) and domestic hot water (DHW) production, showing up to 22 % COP increase for GA-mode and SA-mode. As a further step, the study investigates the effect of varying the number of PV-T modules and borehole heat exchangers on the heat pump performance. The simultaneous use of two energy sources always results in improved system performance even with limited PV-T or BHE heat transfer areas.

1. Introduction

In recent years, European Directives have increasingly highlighted the use of heat pumps as promising renewable solutions to address energy efficiency and reduce greenhouse gas emissions [1]. One of the most widely adopted heat pump systems in buildings is the air-source heat pump (ASHP), appreciated for its easy installation process, reduced energy usage, substantial energy-saving potential, and environmentally friendly design [2]. However, the performance of the ASHPs is strongly affected by air temperature variations across seasons and daily cycles, which declines as the air temperature drops, notably when the heat demand is higher. Furthermore, a combination of the low air temperature and high relative humidity can cause frost formation on

☆ This article is part of a special issue entitled: 'HP with natural fluids' published in Applied Thermal Engineering.

* Corresponding author at: University of Padova, Department of Industrial Engineering, Via Venezia 1, 35131 Padova, Italy.
E-mail address: marco.azzolin@unipd.it (M. Azzolin).

https://doi.org/10.1016/j.applthermaleng.2025.126533
Received 30 November 2024; Received in revised form 1 March 2025; Accepted 17 April 2025
Available online 18 April 2025

Nomenclature

Abbreviations

ASHP	Air source heat pump
BHE	Borehole heat exchanger
COMP	Compressor
COP	Coefficient of performance
DHW	Domestic hot water
DSHP	Dual-source heat pump
DX	Direct-expansion
EEV	Electronic expansion valve
FCHE	Finned coil heat exchanger
GA-DSHP	Ground-air dual-source heat pump
GC	Gas-cooler
GSHP	Ground source heat pump
HP	Heat pump
IDX	Indirect-expansion
IHE	Internal heat exchanger
PUMP	Circulation pump
PV	Photovoltaic
PV-T	Photovoltaic-thermal
REC	Low-pressure receiver
SA-DSHP	Solar-air dual-source heat pump
SAHP	Solar-assisted heat pump
SL	Secondary loop
SH	Space heating

Symbols

A	Area [m^2]
c	Specific heat capacity [J kg^{-1} K^{-1}]
C	Thermal capacity [J K^{-1}]
d	Diameter [m]
D	Distance [m]
GTI	Global tilted irradiance [W m^{-2}]
h	Specific enthalpy [J kg^{-1}]
H	Total enthalpy [J]
HTC	Heat transfer coefficient [W m^{-2} K^{-1}]
L	Length of the borehole [m]
m	Mass [kg]
$\dot{m}$	Mass flow rate [kg s^{-1}]
Nu	Nusselt number [-]
p	Pressure [Pa]
P	Electrical Power [W]
Q	Heat flow rate [W]
r	Radius [m]
R	Thermal resistance [K W^{-1}]
t	time [s]
T	Temperature [°C]
V,v	Volume [m^3]
x	Vapor quality [-]
ρ	Density [kg m^{-3}]
λ	Thermal conductivity [W m^{-1} K^{-1}]
ΔT	Temperature difference [K]

Subscripts

b	Borehole
cond	Conduction
e	External
eq	Equivalent
evap	Evaporation
exp	Experimental
f	Fluid
g	Grout
i	Internal
l	Liquid
num	Numerical
out	Outlet
p	Pipe
r	Refrigerant
s	Soil
tot	Total
v	Vapor
w	Water

the ASHP evaporator and reduce the evaporator efficiency and subsequently the COP of the system [3,4]. To mitigate the limitations of the air source on heat pump performance, alternative heat sources can be exploited, such as geothermal energy in ground-source heat pumps (GSHP) and solar irradiance in solar-assisted heat pumps (SAHP) [5]. These alternatives, both GSHP and SAHP, can operate in two configurations: direct expansion (DX), in which the refrigerant is circulated directly through boreholes or solar collectors, where it undergoes evaporation; indirect expansion (IDX), by using a secondary fluid that is circulated through boreholes or solar collectors to absorb heat, which is then transferred to the refrigerant via a heat exchanger, enabling its evaporation [6].

In the case of GSHPs, DX-GSHPs offer the advantages of lower initial installation costs, improved energy performance, elimination of secondary pumps, and reduced operational expenses compared to IDX-GSHPs, also known as secondary loops [5,7]. Additionally, when compared to ASHP, considering a long-term techno-economic analysis, Hakkaki-Fard et al. [8] demonstrated that properly sizing a DX-GSHP system, with vertical U boreholes, can result in a 50 % reduction in energy consumption with respect to ASHP. However, due to the high installation cost, the payback period for the DX-GSHP is 15 years longer compared to ASHPs. With regards to carbon dioxide as the refrigerant, Choi et al. [9] analytically compared the performance of a DX-GSHP assisted with solar collectors, using R22 or CO_2 as refrigerants under varying conditions. It was found that the COP of the CO_2 DX-GSHP is about 30 % lower compared to the R22 DX-GSHP under various temperature conditions. Austin et al. [10] numerically investigated a DX-GSHP working with CO_2 in a transcritical cycle. After optimization of the system parameters including gas cooler size, mean evaporation temperature, superheating and number/length of evaporator circuits, the optimized system resulted in an 18 % increase in both COP and heating capacity compared to the initial baseline system. When considering an IDX-GSHP, Bordignon et al. [11] numerically analysed the performance of a reversible cascade system working with R134a and R410A. A water-glycol mixture was used to exchange heat with the ground. The simulations were carried out for various locations including Helsinki, Strasbourg, and Athens showing seasonal coefficients of performance equal to 2.48, 2.53, and 2.86 respectively.

Similarly, SAHPs exploit solar irradiance captured by solar thermal collectors as a renewable heat source. In DX-SAHP configuration, the refrigerant directly absorbs the solar irradiance eliminating the use of water pumps and internal heat exchangers, decreasing the risk of corrosion and freezing inside the collectors [12]. A more innovative approach for increasing the efficiency of the SAHPs involves the use of photovoltaic-thermal (PV-T) collectors as the evaporator. Although they present a lower thermal efficiency than solar thermal collectors, the cooling of PV cells contributes to reduced overall net consumption due to improved electricity production [13,14]. Chen et al. [15] introduced a DX-SAHP operating in a novel vapor injection autocascade system, in which a solar collector and a finned coil heat exchanger can work

simultaneously as evaporators. The refrigerant used is a low-GWP mixture of R290/R1233zd(E) with 50/50 % mass composition. The authors numerically showed that the developed system increased the COP by about 16 % and the corresponding heating capacity by 18 % compared to conventional systems that rely only on finned coil evaporators.

It is important to note that most of the DX-HP systems examined in the literature utilize HCFC and HFC as refrigerants. Nevertheless, the adoption of natural refrigerants in future heat pumps will become increasingly crucial due to evolving regulations, such as the European Union's F-gas Regulation (EU) 2024/573 [16], which seeks to phase down the use of HFCs within the EU to reduce their environmental impact. Studies on DX-SAHP have implemented both synthetic R410A [17], R32[17], and R134a [18] and natural refrigerants [19,20]. With regards to DX-GSHPs, there are relatively fewer studies on natural refrigerants than synthetic refrigerants such as R22 [21,22] and R410A [23].

A viable alternative to relying on a single energy source is the use of multisource heat pumps, which can exploit different low-temperature energy sources using distinct evaporators.

Sazon et al. [24] numerically investigated an IDX solar-assisted ground-source CO_2 heat pump using solar collectors (SCs) and BHEs as evaporators. The authors compared different configurations of the proposed heat pump: SCs and BHEs in series and SCs and BHEs in parallel. Model results demonstrated that the series configuration with BHEs after the SCs outperformed the other configurations in terms of seasonal performance factor. Other possible configurations are ground-air and solar-air, coupling ground source or solar source with air to overcome limitations which each source imposes. Pelella et al. [25] numerically examined the thermo-economic optimization of a three-source heat pump (air, ground, and solar) operating with propane as the refrigerant. In their study, the refrigerant flows directly to the finned coil evaporator (air), while SCs and BHEs operate in an indirect-expansion mode using a secondary loop, showing the suitability of ground energy for colder climates and solar for warmer. Also, they investigated the possibility of optimizing the system to increase the seasonal coefficient of performance from 3.43 to 11.76 depending on the location and initial costs.

The advantage of ground-air dual-source heat pumps (GA-DSHP) lies in reduced costs of drilling compared to traditional GSHPs. In fact, combining the borehole evaporator with an air evaporator allows for smaller borehole fields as part of the energy can be extracted from the air source. Grossi et al. [26] reported a 15 –55 % reduction when using an IDX-GA-DSHP compared to the borehole field required for conventional GSHPs with the same heating capacity. Siren et al. [27] numerically compared an IDX-GSHP with an IDX-GA-DSHP, showing that the IDX-GA-DSHP outperforms and reduces the space needed for the bore field. According to the literature, GSHPs are more commonly coupled with solar collectors, auxiliary heating systems, and thermal storage rather than air [28].

Another possibility relies on the use of solar-air dual-source heat pumps (SA-DSHP) which combine the use of solar and air sources. Li et al. [29] compared, experimentally and numerically, the performance of an IDX-SA-DSHP and an ASHP. The results showed the higher performance of the SA-DSHP, enhancing both technical and economic performance compared to the ASHP pump during the heating season. Moreover, Qu et al. [30] experimentally studied the characteristics of an IDX-SA-DSHP with PVT evaporators demonstrating that the electrical conversion efficiency can be improved by 10.3 %. Zanetti et al. [20] have experimentally and numerically investigated a DX-SA-DSHP working with CO_2 as the refrigerant circulating within either PV-T modules or the finned coil heat exchanger, demonstrating an 8 % increase in electrical production due to the better cooling of PV-Ts.

Regardless of the energy sources considered, DSHPs in series configuration must switch between energy sources to ensure maximum performance under varying environmental conditions [26]. However, this switching requires a dedicated control logic to optimize the selection and utilization of each source [31,32]. A viable option that has been proven to be effective is to operate both energy sources simultaneously. Despite its potential benefits, the simultaneous use of different energy sources in DSHPs remains almost unexplored in the available literature, highlighting a gap that warrants further investigation. In a previous work [33], it has been experimentally and numerically addressed the advantages of running a carbon dioxide DX-SA-DSHP with simultaneous operation of solar and air sources evaporators, demonstrating that working in simultaneous mode allows for more flexibility and increased system COP compared to both air mode and solar mode only.

The present literature review indicates that various configurations of dual-source heat pumps have been explored. However, studies on three-source heat pumps remain scarce. Additionally, direct expansion evaporators have received less attention compared to indirect systems, particularly in combination with borehole heat exchangers and natural refrigerants. To the best of the authors' knowledge, no study has yet investigated the use of direct expansion evaporators to exploit multiple renewable energy sources simultaneously.

In order to address this gap in the literature, the present study proposes a multisource direct expansion heat pump using CO_2 as a natural refrigerant and three renewable low-temperature heat sources. In particular, the system is equipped with three direct expansion evaporators (avoiding the use of a secondary fluid): a finned coil heat exchanger for the air source, a PV-T collector for the solar source, and a U-tube borehole heat exchanger for the ground source. The finned coil evaporator is fed in dry expansion, while the solar and ground evaporators operate in flooded mode, overcoming possible maldistribution problems of the mass flow rate. Two configurations of the multisource heat pump are investigated: solar-air mode (SA-mode) with finned coil and PV-T collectors running simultaneously and ground-air mode (GA-mode) with finned coil and BHE running simultaneously. The multisource system operates as a DSHP in each mode. It is important to note that this configuration is different from all existing parallel and series setups found in the literature. A comprehensive numerical model of the heat pump system has been developed and implemented to evaluate the comparative performance of the GA-mode and SA-mode against the conventional air-source mode. This model facilitates a systematic analysis under different thermal load conditions and varying environmental parameters. Specifically, the models of the finned coil and BHE evaporators working with CO_2 have been validated against measurements from ad-hoc experimental tests and from the literature, respectively. The results allow for the evaluation of the performance of this novel multisource heat pump under different working modes (GA-mode, SA-mode, and Air-mode) and scenarios (in terms of both thermal loads and environmental conditions).

2. Heat pump description

The heat pump studied in this work is a direct expansion multisource heat pump, working with CO_2 as the refrigerant, that can exploit three renewable heat sources: solar, air, and ground. Fig. 1 shows the layout of the multisource heat pump system (a) and the logarithmic pressure-enthalpy diagram representing the thermodynamic cycle at design conditions (b). The main components of the system are the compressor (COMP), the gas cooler (GC), the internal heat exchanger (IHE), the electronic expansion valve (EEV, which acts as a backpressure valve that controls the high-pressure by varying its aperture), and the low-pressure receiver (REC). The heat pump is equipped with three evaporators, which are used to exploit the different thermal sources: a finned coil heat exchanger (FCHE), three PV-T collectors, and a U-tube borehole heat exchanger (BHE). Two configurations of this multisource heat pump are studied: solar-air mode (SA-mode) in which the finned coil and PV-T evaporators operate simultaneously, and ground-air mode (GA-mode) in which the finned coil and BHE evaporators run simultaneously.

Following the system layout (Fig. 1a) and the corresponding log(p)-h

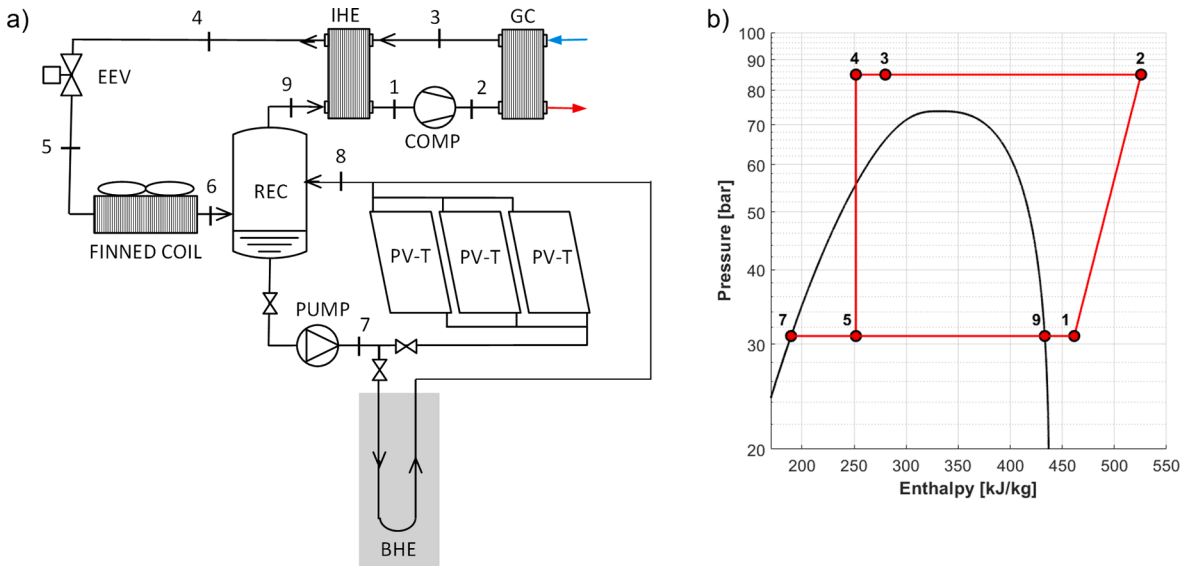

Fig. 1. a) Layout of the multisource heat pump system and b) thermodynamic cycle at the design condition plotted in a log(p)-h diagram.

diagram (Fig. 1b), the superheated refrigerant (point 1), is compressed and sent to the GC to be cooled down. It then passes through the IHE, where it undergoes further subcooling (point 3). After expansion in the EEV, the refrigerant enters the two-phase region and evaporates inside the FCHE (point 5). With an increased vapor quality, the CO_2 enters the REC, where the two-phase mixture separates into vapor and liquid due to density differences. At point 7, liquid CO_2 is taken from the bottom of the REC and directed either to the borehole heat exchanger (BHE) in GA-mode or to the PV-T collectors in SA-mode. After the evaporation process, the refrigerant returns to the REC at point 8. Finally, the saturated vapor (point 9), which is firstly superheated through the IHE, is drawn back into the compressor at point 1. This arrangement allows the FCHE evaporator and the PV-T or BHE evaporators to operate simultaneously. Notably, the three different evaporators (FCHE, PV-T, BHE) and the REC operate at the same pressure level. The low-pressure receiver controls the low-pressure due to the conservation of the mass and energy of the CO_2 inside it [14].

The mass balance can be expressed as:

$$\frac{dm_{REC}}{dt} = \frac{d}{dt}[\rho_l V_l + \rho_v (V_{REC} - V_l)] \tag{1}$$

where V_{REC} and V_l are the volume, respectively, of the receiver and of the CO_2 in liquid phase, ρ_l and ρ_v are the densities in liquid and vapor phases. In general, the variation of the refrigerant mass inside the receiver depends on $\dot{m}_{COMP}$ (which is the mass flow rate elaborated by the compressor) and on the flow rate circulating in the solar/ground evaporator $\left(\dot{m}_{PUMP}\right)$. It can be written in terms of enthalpy fluxes as:

$$\dot{m}_{COMP}(h_{in,REC} - h_v) + \dot{m}_{PUMP}(h_{PVT} - h_l) = \frac{dH}{dt} \tag{2}$$

where H is the refrigerant total enthalpy in the receiver and its rate of change over time depends on the quantity of liquid and vapor phases, as follows:

$$\frac{dH}{dt} = \frac{d}{dt}[\rho_l V_l h_l + \rho_v (V_{REC} - V_l) h_v] \tag{3}$$

3. Numerical method and validation

3.1. Modelling of the borehole heat exchanger

Modelling the borehole heat exchanger (BHE) for direct expansion ground-air mode of the multisource heat pump (GA-mode) involves assessing the heat transfer between the circulating refrigerant and the borehole. The heat transfer within the BHE is crucial for an accurate physical model. In this study, the refrigerant is modelled in terms of enthalpy change along the circuit and integrated with the rest of the system geometry using a thermal resistance and capacity model (TRCM). The properties of the fluids are derived using Refprop 10.0 [34].

3.1.1. Heat transfer

To model the refrigerant flow in a U-tube and its interaction with the rest of the borehole, a quasi-3D approach to thermal resistance and capacity is considered. The model takes into account the enthalpy changes of the fluid as it undergoes heat transfer, which is achieved through two primary mechanisms. Within the fluid (CO_2), heat is transferred by convection. Simultaneously, conduction is responsible for transferring heat from the adjacent materials, the grout, and the soil surrounding the borehole. This dual approach ensures a comprehensive representation of the thermal interactions between the fluid, grout, and soil. The TRCM is schematically shown in Fig. 2.

This approach allows the time derivative of the temperature for a given control volume to be determined by the rate of internal energy change, expressed as:

$$C\frac{dT}{dt} = \frac{\Delta T}{R} \tag{4}$$

where C represents the thermal capacity of the node, ΔT and R represent the temperature difference and the thermal resistance between the two nodes, respectively. For a network of multiple nodes, the generalized equation is defined as:

$$C_j\frac{dT_j}{dt} = \sum_{k=1}^{n_j}\frac{T_k - T_j}{R_k} \qquad \forall j = 1\cdots n \tag{5}$$

where n is the total number of nodes, j is the node index, n_j is the number of adjacent nodes to j, and k is the neighbour node. In this way, the heat transfer from and to each component of the borehole can be calculated. In this study, the single U-loop BHE for a GA-mode is modelled using the method developed by Bauer et al. [35].

3.1.2. Thermal resistances and thermal capacities

The thermal resistance between the fluid flowing inside tubes and the grout zone (R_{fg}) is calculated as follows:

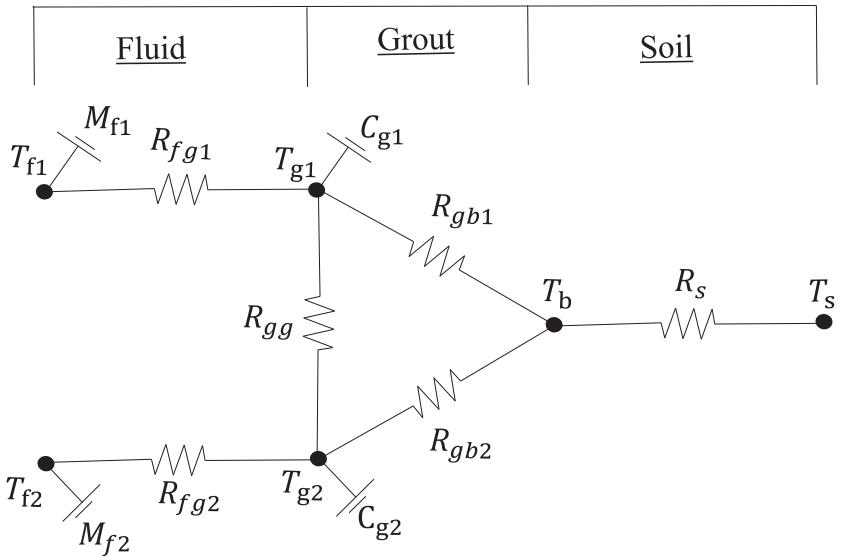

Fig. 2. Network of the thermal resistances (R) and capacities (C) for one layer of the BHE.

$$R_{fg} = R_f + R_{cond,p} + R_{cond,g} \tag{6}$$

where R_f is the convective thermal resistance of the fluid calculated from the Nusselt number (Nu). $R_{cond,p}$ and $R_{cond,g}$ are the conductive thermal resistances of the pipes and the grout, respectively. These thermal resistances are calculated by the following equations:

$$R_f = \frac{1}{\mathrm{Nu}\ \lambda_f\ \pi} \tag{7}$$

$$R_{cond,p} = \frac{\ln\left(\frac{d_e}{d_i}\right)}{2\pi\lambda_p} \tag{8}$$

$$R_{cond,g} = k\ R_g \tag{9}$$

The thermal resistance between the grout zone and the borehole wall (R_{gb}) is calculated as:

$$R_{gb} = (1-k)\ R_g \tag{10}$$

The thermal resistance between the two grout zones is calculated as:

$$R_{gg} = \frac{2R_{gb}\left(R_{ar} - 2kR_g\right)}{2R_{gb} - R_{ar} + 2kR_g} \tag{11}$$

With the thermal resistance of grouting material (R_g) and the thermal resistance between the outer wall of the tubes and borehole wall as follows (R_{ar}), respectively:

$$R_g = \frac{\operatorname{arcosh}\left[\frac{d_b^2+d_a^2+s^2}{2d_b d_a}\right]}{2\pi\lambda_g} \times \left(1.601 - 0.888\frac{s}{d_b}\right) \tag{12}$$

$$R_{ar} = \frac{arcosh\left[\frac{2s^2-d_a^2}{d_a^2}\right]}{2\pi\lambda_g} \tag{13}$$

Finally, x is the parameter used for locating the centre of the mass of the grout, calculated as:

$$x = \frac{\ln\left(\frac{\sqrt{d_b^2+2d_a^2}}{2d_a}\right)}{\ln\left(\frac{d_b}{\sqrt{2}d_a}\right)} \tag{14}$$

The thermal resistance of the soil (R_s) is defined as follows:

$$R_s = \frac{1}{2\pi\lambda_s}\ln\left(\frac{r_m}{r_b}\right) \tag{15}$$

Where λ_s is the thermal conductivity of the soil, r_b is the radius of the borehole and r_m is the average radius between the borehole wall and undisturbed soil.

The Nusselt number for calculation of the fluid thermal resistance is estimated by the convective heat transfer coefficient (HTC) of the fluid:

$$Nu = \frac{2r_{pi}\mathrm{HTC}}{\lambda_f} \tag{16}$$

where λ_f represents fluid thermal conductivity. For CO_2 in two-phase conditions inside pipes, h is calculated using the correlation developed by Cheng et al. [36]:

$$\mathrm{HTC} = 2{\cdot}10^{-8}\ \mathrm{Re}_H^{1.97}\ \mathrm{Pr}_V^{1.06}\ Y^{-1.83}\ \frac{\lambda_V}{d_{eq}} \tag{17}$$

Where the homogenous Reynolds number Re_H and the correlation factor Y are expressed as:

$$Re_H = \frac{Gd_{eq}}{\mu_V}\left[x + \frac{\rho_V}{\rho_L}(1-x)\right] \tag{18}$$

$$Y = 1 - 0.1\left[\left(\frac{\rho_V}{\rho_L} - 1\right)(1-x)\right]^{0.4} \tag{19}$$

where G is the mass flux of the refrigerant. On the other hand, for single-phase flow, the convective heat transfer coefficient HTC is evaluated according to the equation developed by Gnielinski [37]. The equivalent diameter d_{eq} is defined as

$$d_{eq} = \sqrt{\frac{4A}{\pi}} \tag{20}$$

where A is the cross-sectional area of the flow channel.

Regarding the thermal capacities of the network depicted in Fig. 2, the capacity of the soil has been neglected, while the thermal capacity of the grout is defined by the following equation:

$$C_g = \rho_g \frac{\pi}{4}\left(\frac{d_b^2}{2} - d_a^2\right) c_{p,g} \tag{21}$$

3.1.3. Enthalpy change

The governing equation for the enthalpy changes of the fluid within the circuit during time is derived from the energy balance of an infinitesimal element of the fluid of the BHE. For all layers, it is expressed as:

$$m_j \frac{\mathrm{d}h_j}{\mathrm{d}t} = \frac{T_{g,j} - T_{f,j}}{R_{fg}} - \dot{m}_f\left(h_{out,j} - h_{in,j}\right) \qquad \forall j = 1 \cdots n_z \tag{22}$$

Corresponding to the enthalpy change affected by heat transfer on the right-hand side and the enthalpy change due to advection on the left-hand side. In fact, $h_{in,j}$ and $h_{out,j}$ represent the specific enthalpy of the fluid entering and exiting from a general node j, which are used to evaluate the bulk enthalpy of the fluid as follows:

$$h_{f,j} = \frac{\left(h_{in,j} + h_{out,j}\right)}{2} \qquad \forall j = 1 \cdots n_z \tag{23}$$

T_{fj} is the fluid temperature along the pipe calculated from pressure and specific enthalpy using Refprop 10.0, and m_j is the mass associated with each volume of the refrigerant element, assumed to be an average temperature between the fluid inlet and outlet of the element

$$m_j = \rho_j \nu_j \qquad \forall j = 1 \cdots n \tag{24}$$

3.1.4. Algorithm and convergence factors of the BHE

Temperature gradients within the borehole are generally high in the vertical direction, primarily due to fluid heat transfer. To improve numerical stability, the total length of the borehole is divided equally into different layers. In all layers, the heat fluxes among nodes are calculated for each node. Then, having two values of the heat fluxes at the grout nodes, the convergence criteria require the equalization of the heat fluxes calculated for each layer at these nodes. Fig. 3 presents a general layer of the network, the heat transfer between the different temperature nodes of the network is calculated considering the general equation below for two points of the network after the calculation of the temperatures.

$$Q = \frac{\Delta T}{R} \tag{25}$$

Nodes representing the temperatures of the grout, namely T_{g1} and T_{g2}, are central for the calculation of the balance of the heat fluxes transferred among nodes which are calculated once for the neighboring nodes (T_{f1} and T_b for T_{g1}, T_{f2} and T_b for T_{g2}) and once for T_{g1} and T_{g2}. When these criteria are satisfied for the whole borehole, convergence is achieved for the fluid evaporating temperature at every layer along the tube, as well as for the temperatures of the grout and borehole boundary.

Fig. 4 illustrates the flowchart with the algorithm used in the BHE evaporator model. The inputs of the model are the enthalpy and the pressure at the inlet of the U-tube, the undisturbed soil temperature, and the geometrical information of the borehole. It has been assumed that the pressure losses are negligible, so the pressure is constant during the evaporation process. The model calculates the fluid condition inside the borehole (enthalpy, vapor quality, and temperature), the heat flux, and the temperature of the grout and borehole wall.

3.1.5. Steady-state validation of the BHE evaporator numerical model

To investigate the accuracy and reliability of the newly developed BHE evaporator model when it is used as a direct expansion evaporator of CO_2, the results of the simulations are compared to the experimental data of Badache et al. [38].

The BHE consists of 30 m vertical boreholes, arranged in parallel, with a diameter of 78 mm. Inside each borehole, there is a single copper

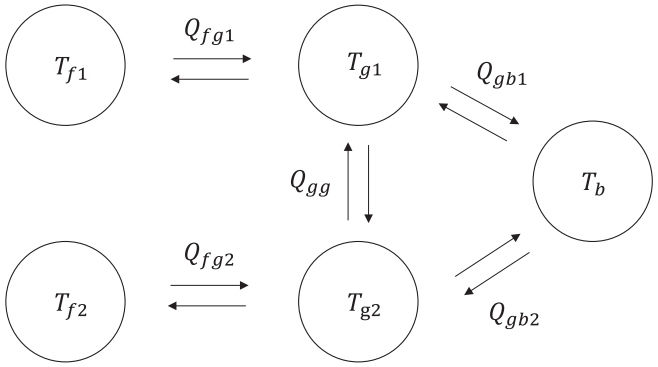

Fig. 3. Network of the heat fluxes for one layer of the BHE.

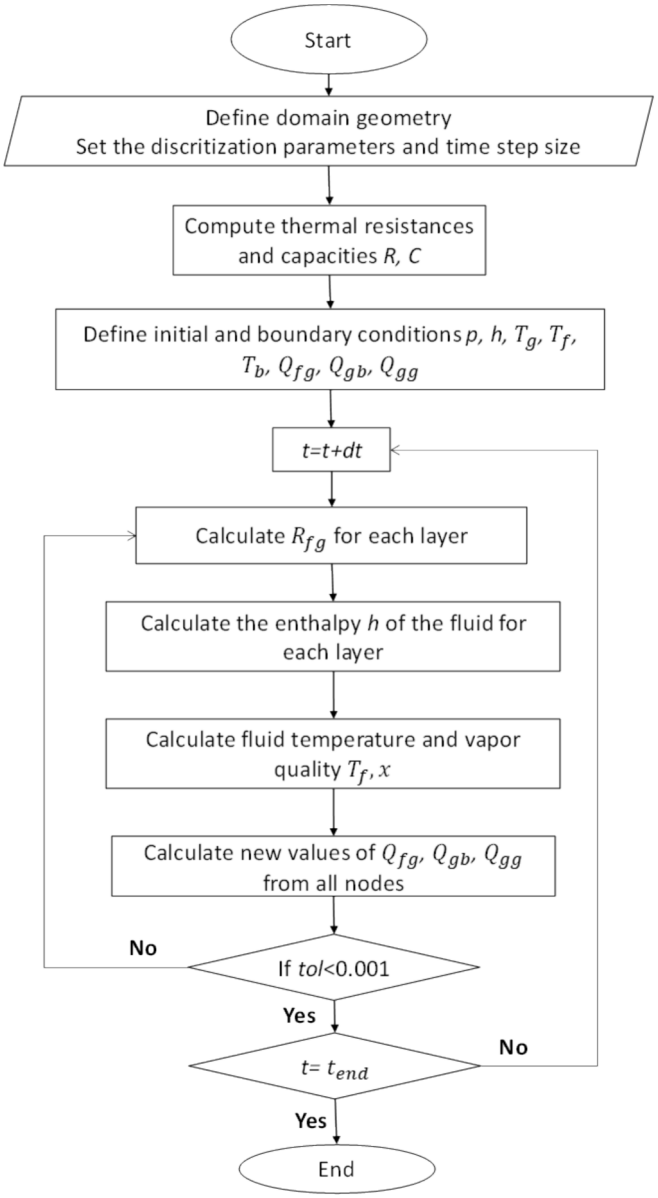

Fig. 4. Flowchart algorithm of the BHE evaporator model.

U-tube, where the refrigerant flows inside. The original U-tube has two different internal diameters in the downward flow direction and the upward flow direction, for simplicity an average value of 5.6 mm is assumed. Grout with a nominal conductivity of 0.8 W/(m K) was used for the filling material inside the borehole. The geometrical characteristics of the borehole reported in [38] and as inputs for the simulations are summarised in Table 1. In particular, the undisturbed soil temperature (assumed at a 5 m distance from the borehole wall) of the simulation is equal to 9.5 °C along the depth for all simulations. However, for Badache et al. [38] a soil temperature profile from 2 °C to 9.5 °C was considered for the first 5 m of depth.

The other input parameters needed for performing simulations are the number of boreholes, evaporating temperature, refrigerant mass flow rate, and the main output used for comparison is the total heat exchanged in BHEs. The total heat exchanged Q_{BHE} is defined as the difference between the enthalpies at the inlet and outlet of one borehole:

$$Q_{BHE} = \dot{m}_f(h_{out} - h_{in}) \tag{26}$$

Q_{BHE} was calculated for one BHE. In the case of multiple boreholes, the value of Q_{BHE} is multiplied by the number of boreholes, given that the refrigerant flow is distributed in parallel for each borehole and there is no mutual effect among them. The percentage deviation between the predicted result and the experimental data was evaluated as:

$$Error = \frac{|Q_{BHE,exp} - Q_{BHE,num}|}{Q_{BHE,exp}} \times 100 \tag{27}$$

Fig. 5 shows the validation of the BHE model, where the evaporator capacity calculated by the model (num) is compared to the experimental measurement by Badache et al. [38] (exp). The comparison highlights the good agreement between experimental and simulated results, demonstrating the model's reliability in predicting CO_2 evaporation inside the BHE with an average error on the evaporating capacity equal to 4.1 %.

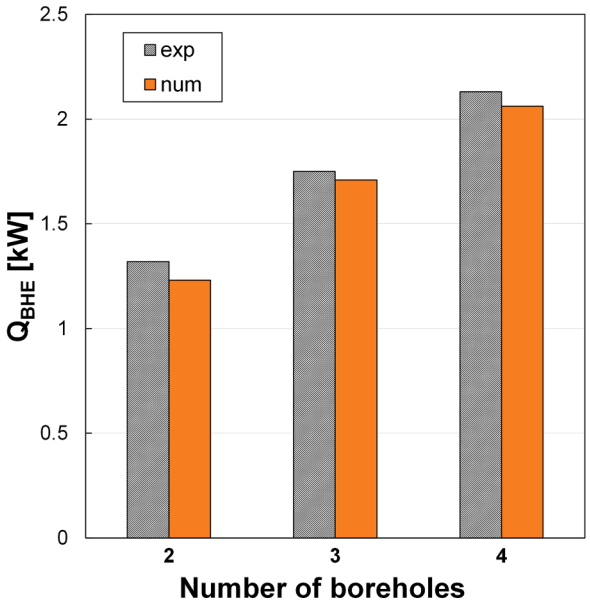

Fig. 5. Comparison of the BHE evaporating capacity calculated by the numerical model (num) against experimental data by Badache et al. [38] (exp) for various numbers of boreholes. According to [38] the input values for the mass flow rate and the evaporating temperature are equal to 6.61 g/s and −2.55 °C, 8.02 g/s and −1.66 °C, 10.6 g/s and −0.62 °C respectively for 2, 3, and 4 boreholes.

3.2. Modelling of the heat pump components

The models of the main heat pump components have been developed using MATLAB®. Each of these models is combined to interact in a principal model to evaluate the operation of the heat pump fluxes in all environmental conditions. The model can simulate both steady-state and dynamic conditions. Table 2 summarizes the modelling strategy employed for each component.

The results of the models of these components have been validated against experimental data in previous studies: the finned coil evaporator in [39], the gas cooler in [40], the low-pressure receiver in [41], and the internal heat exchanger in [33]. For the SA-mode, the direct expansion PV-T evaporator model operating with CO_2 has already been presented and validated in [14].

Table 2
Details of the modeling of the main components of the heat pump system.

Component	Modelling
Compressor	Modelled using three polynomial equations reported with their coefficients in the Appendix, according to [20].
Gas cooler	Modelled using a distributed parameter approach with a finite discretization of the volume, where the continuity, momentum, and energy equations are solved.
Internal heat exchanger	
Finned coil evaporator	
PV-T evaporator	
Low-pressure receiver	Modelled using mass and energy balances to find the evaporating temperature.

The modelling of the solar-air dual-source heat pump was previously described and developed in [33]. In the current study, the model of the heat pump has been updated by integrating a newly developed model of a direct expansion borehole heat exchanger working as an evaporator.

Table 1
Borehole characteristics from Badache et al. [38] for the BHE evaporator model validation.

Borehole components	Variables	Units	Value	Borehole layout
Length of the tube	L	m	30	
Borehole radius	r_b	mm	39	
Tube external diameter	d_e	mm	7.2	
Tube internal diameter	d_i	mm	5.6	
Distance between the two axes of the two tubes	2D	mm	23	
Grout thermal conductivity	λ_{grout}	W/(m K)	0.8	
Pipe thermal conductivity	λ_{pipe}	W/(m K)	400	
Soil thermal conductivity	λ_{soil}	W/(m K)	2.65	
Density times specific heat capacity of the grout	$\rho_g c_g$	MJ/(kg K)	2.25	
Distance from the borehole wall to the undisturbed soil	D_s	m	5	

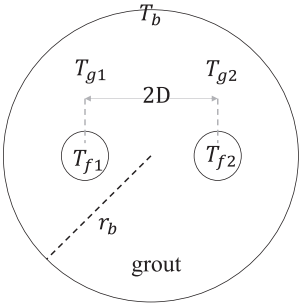

This updated configuration allows the refrigerant to be sent directly to the boreholes.

3.3. Numerical procedure

Building upon the SA-mode model developed in [33], the BHE sub-model has been integrated into the overall heat pump model. This integration allows the entire heat pump model to exploit either the solar-air or the ground-air sources simultaneously. Fig. 6 summarizes the overall algorithm of the heat pump model, illustrating its capability to operate in either SA-mode or GA-mode. The model inputs refer to ambient conditions (such as T_{air}, GTI, T_{soil} and air velocity) and the operative conditions of the heat pump (including compressor speed, high-pressure, fan speed, circulation pump speed, and water temperature at the gas cooler). The iterative procedure is as follows:

1. Begin the simulation by setting the initial guess for the evaporating temperature (T_{evap}) and the superheating level at the compressor suction.
2. Implementing the compressor model to determine the refrigerant flow rate, condensation pressure, and isentropic compressor efficiency, which estimates the enthalpy at the compressor outlet.
3. Apply the gas cooler model to calculate the heating capacity and the outlet temperature of the fluid.
4. The internal heat exchanger model determines the refrigerant temperatures at the outlet of the high-pressure and low-pressure sides.
5. Repeating steps 2 through 4. until the difference between the calculated and assumed low-pressure outlet temperature is within 0.01 K.
6. For the first evaporation process, the finned coil heat exchanger model is used to calculate evaporating capacity, the refrigerant vapor quality and the enthalpy at the outlet of the finned coil, the latter corresponds to the enthalpy at the inlet of the low-pressure receiver.
7. For the second evaporation process, the model allows the selection of the appropriate evaporator to calculate the evaporating capacity, refrigerant vapor quality, and enthalpy at the evaporator outlet. The selection depends on the operational mode: in GA-mode, the BHE model is employed, and in SA-mode, the PV-T model is utilized. This selection ensures that the appropriate calculations are performed based on the active heat source configuration.
8. The evaporating temperature (T_{evap}) is calculated by solving the energy and mass balance equations in the low-pressure receiver.
9. This procedure is repeated from step (2) to step (8). When the T_{evap} reaches a convergence value lower than 0.01 K, the procedure stops and then COP is calculated:

$$\mathrm{COP} = \frac{Q_{GC}}{P_{tot}} \tag{28}$$

where Q_{GC} is calculated with water side temperatures and mass flow rate at the gas cooler and P_{tot} is the total electric consumption.

After the iterative procedure, the COP of the HP, operating in steady-state conditions, is evaluated. The model can also evaluate the dynamic operation of the heat pump when the environmental conditions change at each time step.

3.4. Dynamic validation of the results in SA-mode

The SA-mode analyzed in this work corresponds to the real SA-DSHP prototype installed at the Department of Industrial Engineering of the University of Padova. It is a direct-expansion CO_2 heat pump that produces a maximum heating capacity of 5 kW in transcritical conditions. Fig. 7 shows the layout of the SA-DSHP prototype, including the measurement sensors installed. The main components of the system are the compressor (COMP), the gas cooler (GC) the internal heat exchanger (IHE), and the electronic expansion valve (EEV, which acts as a backpressure valve that controls the high-pressure level by varying its aperture), one finned coil heat exchanger (FCHE), a low-pressure receiver (REC) and three PV-T collectors working as evaporators. The main characteristics of these components are reported in Table 3. The SA-DSHP can simultaneously exploit two thermal sources in direct

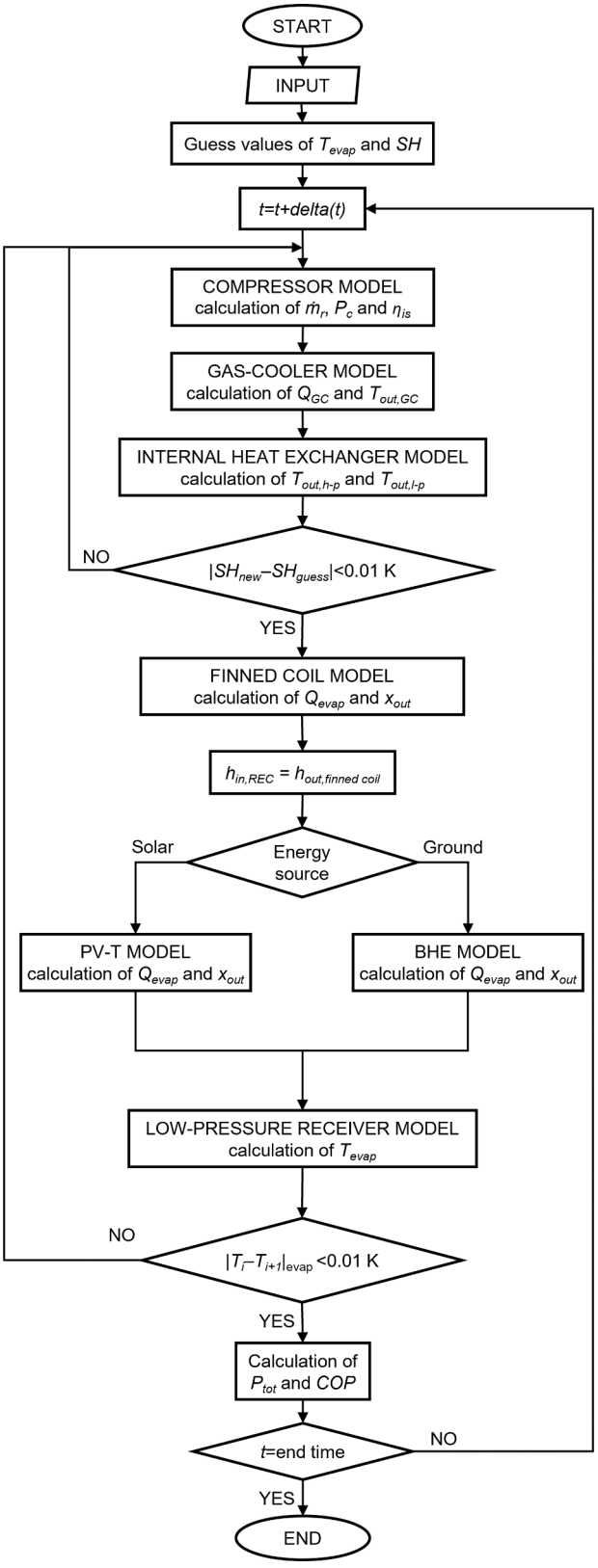

Fig. 6. Flowchart of the multisource heat pump model.

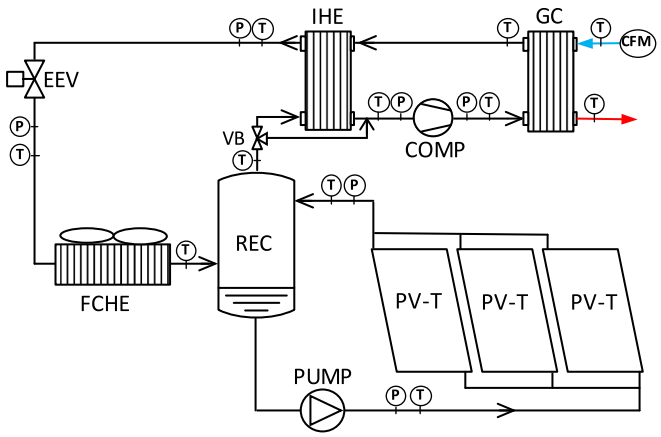

Fig. 7. Layout of the SA-DSHP system. The picture shows the temperature (T), pressure (P), and flow rate (CFM) sensors. COMP is the compressor, GC is the gas-cooler, IHE is the internal heat exchanger, EEV is the electronic expansion valve, FCHE is the finned coil heat exchanger, REC is the receiver, PV-T is the photovoltaic and thermal evaporators, VB is the ball valve.

expansion: the air source, using the finned coil as the evaporator, and the solar source, using the three PV-T collectors as the evaporator. In fact, after the EEV, the refrigerant is directed to the finned coil heat exchanger, where it undergoes the first evaporation process. Subsequently, the refrigerant reaches the low-pressure receiver where the liquid CO_2 is extracted from the bottom by the pump and circulated into the PV-T collectors in flooded mode for the second evaporation process. Notably, the finned coil, the PV-T collectors, and the low-pressure receiver operate at the same pressure level. For more details regarding the description of the experimental apparatus refer to Conte et al. [33].

The SA-mode and GA-mode share all components except for their respective evaporators for the renewable source. For the SA-mode, the numerical model in simultaneous mode has been validated under steady-state conditions in [33] for a SA-DSHP. This section presents some experiments conducted on the SA-DSHP prototype to validate the results of the model during dynamic conditions. As shown in Fig. 7, the refrigerant temperature and pressure conditions along the heat pump circuit were monitored using T-type thermocouples (position denoted as T in Fig. 7) with an uncertainty of ± 0.1 K and pressure transducers (position denoted as P in in Fig. 7) with an uncertainty of ±5 kPa. On the water side, the inlet and outlet temperatures at the gas cooler were measured using two RTD Pt-100 sensors with an uncertainty of 1/10 DIN, while the water mass flow rate was determined using a Coriolis effect flow meter (denoted as CFM in Fig. 7) with an accuracy of ±0.1 % of the reading. Environmental conditions were recorded using an RTD Pt-100 to measure air temperature, and three pyranometers to capture the different components of solar radiation. Two Kipp & Zonen CM11 pyranometers and one Zonen CMP22 equipped with a shading ring were utilized for this purpose. The evaporating temperature was calculated from the pressure measurement at the evaporator inlet. Data acquisition was collected over two hours with a sampling interval of 10 s. The operation conditions of this test were: compressor speed at 50 %, CO_2 circulation pump speed at 40 %, fan speed at 50 %, high pressure maintained at 80 bar, and water temperatures in the gas cooler from 30 °C to 35 °C. During this test, the SA-DSHP was working with the air source and the solar source simultaneously.

Fig. 8 shows the dynamic evolution of the global tilted irradiance (GTI), air temperature (T_{air}) and evaporating temperature ($T_{evap,\exp}$) measured during a partly cloudy day and also the evaporating temperature ($T_{evap,num}$) calculated with the dynamic model. In the first hour (from 10:30 to 11:25), GTI varies significantly in a range from 400 to 800 W/m^2 and then, following an abrupt decrease, it remains under 400 W/m^2 for the remaining testing period. The air temperature increases from 8 °C to 10 °C, during the first hour, and then it remains constant. It can be noticed that, in this case, the evaporating temperature is mainly influenced by solar irradiance, but its variation is damped by the thermal inertia of the PV-T collectors and the finned coil evaporator. Overall, the model can predict the response of the heat pump in simultaneous mode with good accuracy, following the experimental trend. The evaporating temperature is slightly underestimated with an average error of 0.3 K and a maximum difference equal to 0.5 K. These results demonstrate the model's capability to accurately predict experimental outcomes.

4. Design of the multisource heat pump

To design the BHE evaporator for the GA-mode, the north Italy climate condition was selected, with Padova as the reference location, corresponding to an average monthly solar irradiance on the horizontal plane equal to 300 W/m^2 [42], an annual average soil temperature of 13 °C [43], and the average air temperature is considered to be 7 °C. The fixed operating conditions for SA-mode and GA-mode are maximum compressor speed, fan speed equal to 50 %, high-pressure equal to 85 bar, and water temperatures at the gas cooler from 30 °C to 40 °C. The PV-T characteristics of the SA-mode are those reported in Table 3. The photovoltaic (PV) modules utilize multicrystalline silicon cells, each with a nominal power output of 270 W and a total surface area of 1.64 m^2 (dimensions1650 × 992 mm). The plate-and-tube heat exchanger is composed of 15 copper tubes arranged in a serpentine configuration, with an outer diameter of 8 mm, a wall thickness of 1 mm, and a spacing of 80 mm, all bonded to an aluminum absorber plate that is 0.5 mm thick. This aluminum plate covers 75 % of the available space on the back of the PV module and is secured using thermal adhesive. The PV-T collectors are mounted at a 45° tilt angle. The BHE characteristics of the GA-mode are listed in Table 1, with only the length of the BHE as the independent variable. To reduce the costs associated with drilling and installation (accounting also that it is a dual-source heat pump), the design accounted for only one borehole. The outcomes of the design

Table 3
Characteristics of the main components of the heat pump system.

Component	Type	Characteristics
Compressor	Rotary, inverter-driven	Displacement: 3.02 cm^3/rev
Gas cooler	Brazed plate	Plate size: 379 × 79 mm^2 N° of plates: 28
Internal heat exchanger	Brazed plate	Plate size: 377 × 120 mm^2 N° of plates: 4
Throttling valve	Electronic	High-pressure control
Low-pressure receiver	Cylindrical tank	Tank size: 20 L
Liquid circulation pump	Gear pump, variable-speed	Displacement: 0.81 mL/rev
Air evaporator	Finned coil with inverter-driven fan	Tube internal diameter: 9.5 mm
PV-T evaporator	Multicrystalline silicon PV	Nominal power: 270 W Panel size: 1650 × 992 mm^2
	Collector	Tube internal diameter: 6 mm

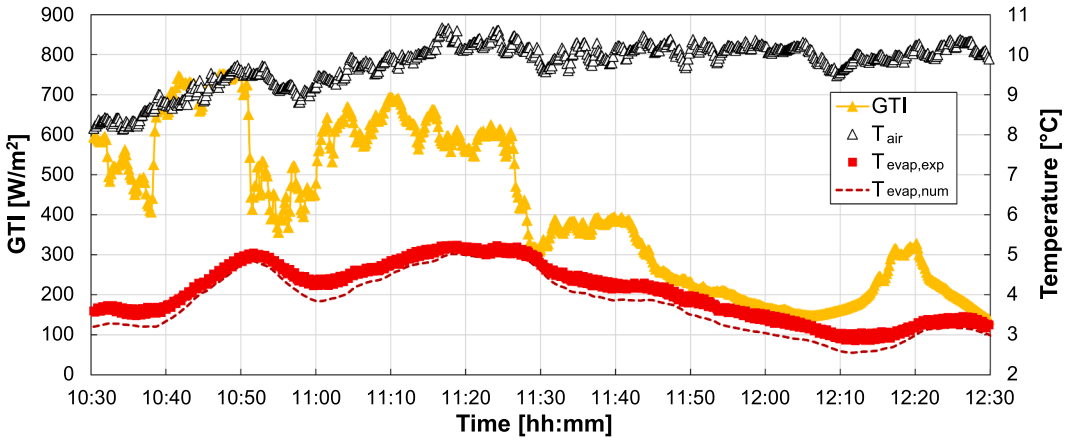

Fig. 8. Dynamic evolution of the experimental (exp) and numerical (num) evaporating temperatures during a partly cloudy day for the SA-DSHP. Experimental values of air temperature and solar irradiance are reported.

Table 4
Main results of the design of the heat pump in SA-mode and GA-mode.

Heat pump	T_{evap}	Q_{FCHE}	$Q_{BHE/PVT}$	Q_{evap}	Q_{GC}	COP
	[°C]	[W]	[W]	[W]	[W]	[-]
Air-mode	−7.3	3160	–	3160	5067	2.78
SA-mode	−4.5	2358	1086	3444	4661	2.95
GA-mode	−4.6	2436	1063	3499	4746	2.98

procedure indicated that a borehole depth of 35 m results in the same evaporating and heating capacity as compared to the SA-mode. Both configurations share an identical air evaporator, which consists of a finned coil heat exchanger comprising four copper tube circuits (10.12 mm outer diameter, 0.35 mm wall thickness) arranged in four rows and 22 columns, with a row spacing of 21.65 mm and a tube spacing of 25 mm. The aluminum fins have 0.12 mm thickness and 3.2 mm spacing.

The main results of the air-mode (working only with FCHE as evaporator), the GA-mode and the SA-mode performance during the design condition are summarized in Table 4. Under these design conditions, the higher evaporating capacity is ensured when the PV-T or the BHE evaporators act as additional thermal sources working simultaneously with the air-source evaporator. The PV-T and BHE evaporators have nominal evaporating capacities that are respectively 53 % and 56 % lower compared to the finned coil evaporator. They are designed with smaller heat transfer areas than the FCHE to explore potential installations in spaces with limited ground or roof availability and to reduce installation costs.

5. Simulations results

This section employs the numerical methods described and validated in Sec. 3 to compare the steady-state performance of the multisource heat pump operating in two configurations: SA-mode and GA-mode, with evaporators working simultaneously. In both configurations, the heat pump has been designed to ensure that the BHE evaporator produces the same evaporating capacity as the PV-T evaporator under specific operating conditions. The analysis then focuses on the effects of various parameters on the performance of the multisource heat pimp in each mode of operation, including temperature demand, environmental conditions, number of PV-T panels and number of boreholes. These factors are examined to provide a comprehensive understanding of the system's performance under different scenarios.

In this section, the COP is defined as a performance indicator based on the heating capacity divided by the total electricity consumption of the heat pump system, including the compressor, the finned coil evaporator fan, and the PV-T and BHE evaporator pump, while excluding the electricity generated by the PV cells.

5.1. Effect of environmental conditions

The developed model enables a comparison of the multisource heat pump working in SA-mode and GA-mode for various heating applications providing insights into the performance under different environmental conditions. In particular, the performance of both configuration modes is affected by the air temperature (T_{air}) because the finned coil evaporator is used simultaneously with the renewable source evaporator. It must be noted that the finned coil evaporator model was validated against experimental data from the climatic conditions of the location where the SA-DSHP prototype is installed (see Sec. 3.4), which includes only air temperatures above 2 °C. Therefore, this study is limited to air temperatures above 0 °C. Furthermore, the performance of the SA-mode also depends on solar irradiance (GTI), while that of the GA-mode depends on soil temperature (T_{soil}). To study the impact of environmental conditions on the two configurations, this section presents the simulation results obtained when varying T_{air} (between 0 °C and 16 °C), T_{soil} (between 5 °C and 15 °C) and GTI (between 100 W/m^2 and 1100 W/m^2), while maintaining fixed the compressor speed at maximum, fan speed set at 50 %, the high-pressure at 85 bar, and the water temperatures at the gas cooler (inlet temperature equal to 30 °C, outlet temperature equal to 40 °C). The circulation pump's speed for the liquid CO_2 was not fixed but allowed to vary. This flexibility ensured that, in any condition, the solar or geothermal evaporator received a refrigerant mass flow rate equal to half of the mass flow rate processed by the compressor.

Fig. 9 shows the simulated map of the COP obtained for the SA-mode (Fig. 9a), as a function of air temperature and global solar irradiance on the tilted plane (GTI), and for the GA-mode (Fig. 9b), as a function of air temperature (T_{air}) and soil temperature (T_{soil}). The *iso*-COP map of the SA-mode (Fig. 9a) demonstrates that, as T_{air} increases from 0 °C to 16 °C and GTI rises from 100 W/m^2 to 1100 W/m^2, the COP exhibits an upward trend from 2.6 to 3.6. However, the slope of this trend differs, with an approximate COP increase of 4.8 % for every 1 K rise in T_{air} and an approximate increase of 2.8 % for every 100 W/m^2 rise in GTI. The increase in GTI exerts a lower influence on the COP than the effect of T_{air} since the PV-T evaporator's nominal evaporating capacity in design condition (T_{air} equal to 7 °C and GTI equal to 300 W/m^2) is 53 % lower compared to that of the finned coil evaporator. Similarly, the *iso*-COP map for the GA-mode (Fig. 9b) indicates that the COP exhibits an increase from 2.6 to 3.4, primarily due to the rise of T_{air} from 0 °C to 16 °C, rather than the increase of T_{soil} from 5 °C to 15 °C. This is evidenced by a rate of approximately 4.3 % for every 1 K of T_{air} increase and approximately 0.9 % for every 1 K of T_{soil} increase. The diminished impact of T_{soil}

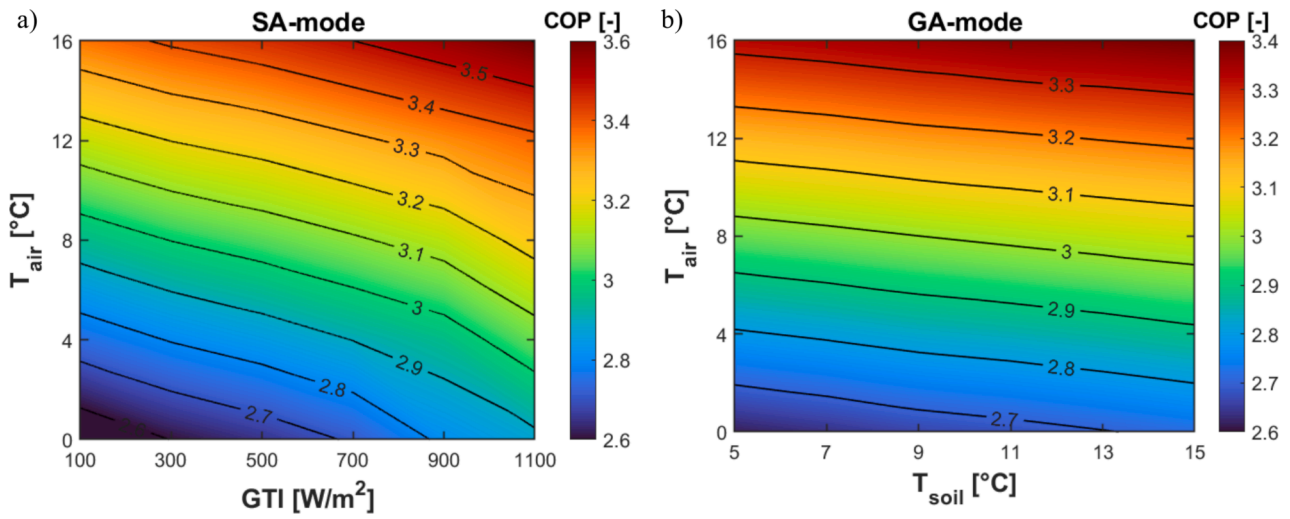

Fig. 9. Maps of the *iso*-COP as a function of (a) air temperature and solar irradiance for the SA-mode and (b) air temperature and soil temperature for the GA-mode.

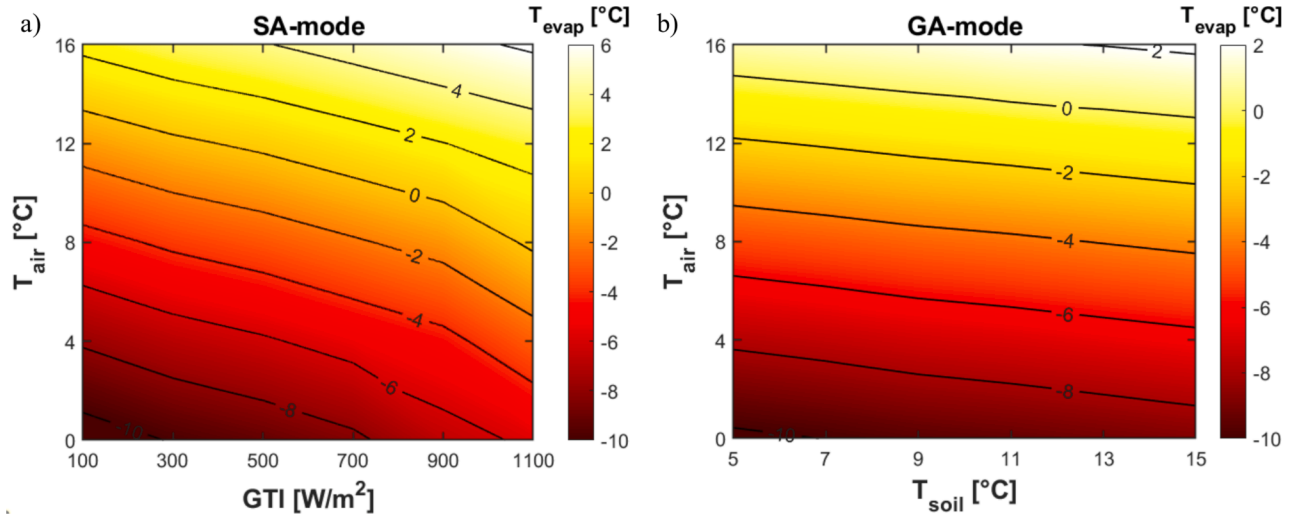

Fig. 10. Maps of the evaporating temperature as a function of (a) air temperature and solar irradiance for the SA-mode and (b) air temperature and soil temperature for the GA-mode.

on the COP relative to T_{air} can be attributed to the 56 % lower evaporating capacity at the design condition (T_{air} equal to 7 °C and T_{soil} equal to 13 °C) of the BHE compared to the finned coil evaporator. To summarize, the impact of solar irradiance and soil temperature on the COP is less pronounced compared to that of air temperature because the number of PV-T panels and the heat transfer area of the BHE were dimensioned to complement and increase the air evaporator's performance rather than to serve as a complete substitute for it.

The evaporation temperature strongly influences the performance of the heat pump. Fig. 10 shows the corresponding map of the evaporating temperature T_{evap} for the SA-mode (Fig. 10a), as a function of T_{air} and GTI, and for the GA-mode (Fig. 10b), as a function of T_{air} and T_{soil}. Similar to the COP trend shown in Fig. 9a, the evaporating temperature of the SA-mode (Fig. 10a) increases with both T_{air} and GTI. In particular, T_{evap} rises by about 0.79 K for every T_{air} increment of 1 K and by about 0.46 K for every GTI increment equal to 100 W/m^2. Similarly, the map for the GA-mode (Fig. 10b) indicates that T_{evap} increases almost linearly with T_{air} and T_{soil}, with a higher effect of T_{air}. In fact, the evaporating temperature rises on average by 0.70 K for an increment equal to 1 K in T_{air} and by 0.14 K for an increment of 1 K in T_{soil}.

For each operation mode with two evaporators simultaneously, it is crucial to understand the contribution of each evaporator to the overall evaporation process. Fig. 11 reports the heat flow rate in each evaporator of the multisource heat pump for both SA-mode (Fig. 11a) and GA-mode (Fig. 11b). The simulations have been performed for different air temperatures (0 °C, 4 °C, 8 °C, 12 °C, and 16 °C), considering a GTI range from 100 to 1100 W/m^2 (Fig. 11a) and soil temperatures ranging from 5 to 15 °C (Fig. 11b). Focusing on the SA-mode (Fig. 11a), the total evaporating capacity, which is the sum of the Q_{PVT} and Q_{FCHE}, increases with both GTI and T_{air}. However, the contributions of the two evaporators exhibit opposite trends as GTI rises: the contribution of the PV-T evaporator increases while the evaporating capacity at the FCHE decreases. This is because when increasing the GTI, the evaporating pressure and temperature increase and this reduces the temperature difference with the air, resulting in a decreasing trend for the evaporating capacity at the FCHE. Instead, when T_{air} rises, both evaporators experience an increase in their evaporating capacity. Specifically, when GTI increases from 100 to 1100 W/m^2, the contribution of PV-T evaporators to the total evaporation process rises from 23 % to 65 % at T_{air} of 0 °C, corresponding to an increase in evaporating capacity from 640 W to 2160 W, and from 20 % to 56 % at T_{air} of 16 °C, with evaporating capacity increasing from 800 W to 2370 W. Considering the GA-mode (Fig. 11b), the total evaporating capacity increases with both T_{soil} and T_{air}. As seen for the SA-mode, the contributions of the two evaporators

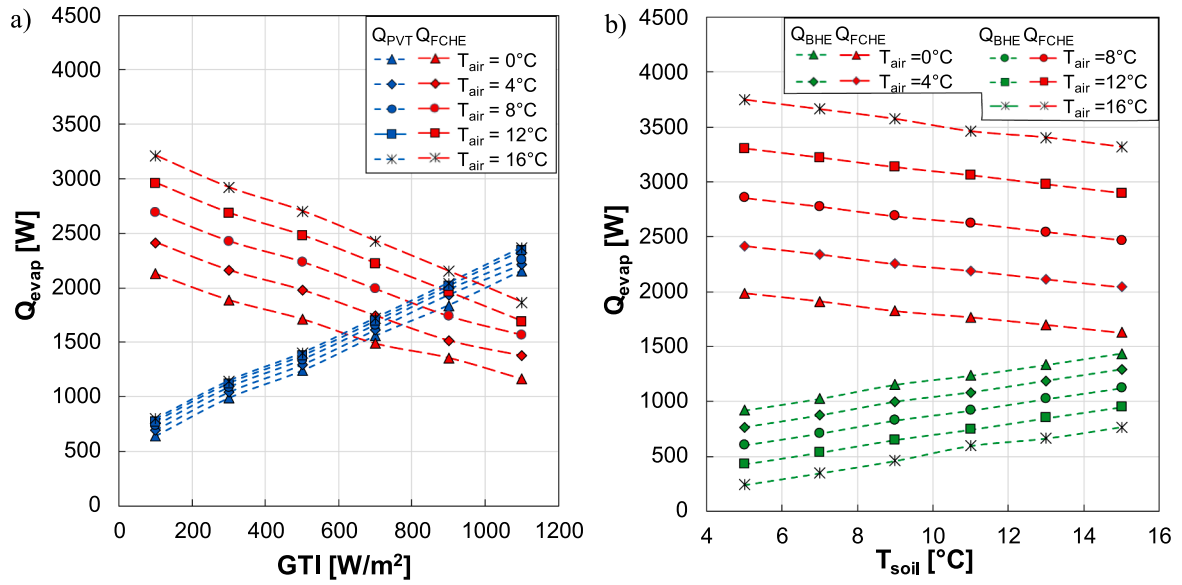

Fig. 11. a) Evaporating capacity Q_{evap} in the PV-T and finned coil (FCHE) evaporators of the SA-mode at varying solar irradiance GTI. b) Evaporating capacity Q_{evap} in the BHE and FCHE evaporators of the GA-mode at varying soil temperature T_{soil}. The results are reported for different air temperatures.

exhibit opposite trends as T_{soil} rises, regardless of T_{air}. Specifically, when T_{soil} increases from 5 °C to 15 °C, the geothermal evaporator's contribution to the total evaporation process rises from 32 % to 47 % at T_{air} of 0 °C, corresponding to an increase in evaporating capacity from 915 W to 1435 W, and from 6 % to 19 % at T_{air} of 16 °C, with capacity increasing from 240 W to 760 W. Due to its smaller heat transfer area, the contribution of the geothermal evaporator is always smaller than that of the finned coil. However, at high T_{soil} (15 °C) and low T_{air} (0 °C), the contributions of the two evaporators become comparable.

As expected, the results indicate that in a multisource heat pump operating in simultaneous mode, the contribution of PV-T collectors (for SA-mode) and BHEs (for GA-mode) to the evaporation process is more significant at low air temperature. Conversely, while their contribution decreases at high air temperatures, it remains beneficial to system performance even with a small collector area or a shallow borehole heat exchanger.

Fig. 12 shows the heating capacity provided by the heat pump for different air temperatures (0 °C, 4 °C, 8 °C, 12 °C, and 16 °C), as a function of GTI ranging from 100 to 1100 W/m^2 in SA-mode (Fig. 12a), and soil temperatures ranging from 5 to 15 °C in GA-mode (Fig. 12b). Focusing on the SA-mode (Fig. 12a), the heating capacity increases with both GTI and T_{air}. Generally, when GTI increases from 100 to 1100 W/m^2, Q_{GC} rises by about 15 % at T_{air} of 0 °C, and by about 3 % at T_{air} of 16 °C. Therefore, GTI has a higher effect when the air temperature is lower. Conversely, T_{air} has a higher effect at low values of GTI. In fact, when T_{air} increases from 0 to 16 °C, Q_{GC} rises by about 30 % at GTI of 100 W/m^2, and by 17 % at GTI of 1100 W/m^2. Considering the GA-mode (Fig. 12b), the heating capacity increases with both T_{soil} and T_{air}, but with different contributions. When T_{soil} increases from 5 to 15 °C, Q_{GC} rises by 4 % at T_{air} of 0 °C, and by 1.5 % at T_{air} of 16 °C. On the other hand, when T_{air} increases from 0 to 16 °C, Q_{GC} rises by 25 % at T_{soil} of 5 °C, and by 22 % at T_{soil} of 15 °C.

5.2. *Effect of water temperature demand in heating applications*

This section aims to evaluate the performance of the multisource heat pump under different characteristics of the water heat demand at the gas cooler. With the other operating conditions maintained constant, simulations were performed for two different water temperature demands specific to different heating applications:

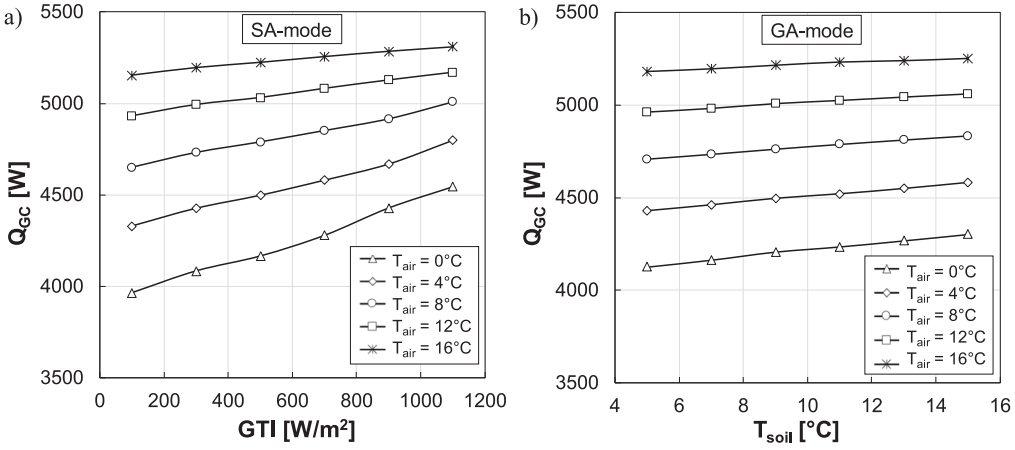

Fig. 12. Heating capacity Q_{GC} during a) SA-mode at varying solar irradiance GTI, and b) GA-mode at varying soil temperature T_{soil}. The results are reported for different air temperatures.

1) Space heating (SH) with water supply temperature from 30 °C to 40 °C.
2) Domestic hot water (DHW) with water supply temperature from 20 °C and 50 °C.

To compare the performance of the multisource heat pump in SA-mode and GA-mode for the mentioned applications with that of the air-mode (heat pump operating with only the air-source), the following operating conditions are fixed: maximum compressor speed, fan speed set at 50 %, high-pressure maintained at 85 bar, the refrigerant mass flow rate inside the solar or geothermal evaporators equal to half of the mass flow rate processed by the compressor, and air temperature equal to 4 °C.

Fig. 13 illustrates the COP, heating capacity and evaporating temperature of the system for the mentioned applications (SH and DHW), considering two opposite environmental scenarios: 1) low contributions of the solar and ground heat sources, corresponding to T_{soil} = 7 °C and GTI = 300 W/m^2 (Fig. 13a-c-e), 2) high contributions of the solar and ground heat sources, corresponding to T_{soil} = 15 °C and GTI = 1100 W/m^2 (Fig. 13b-d-f).

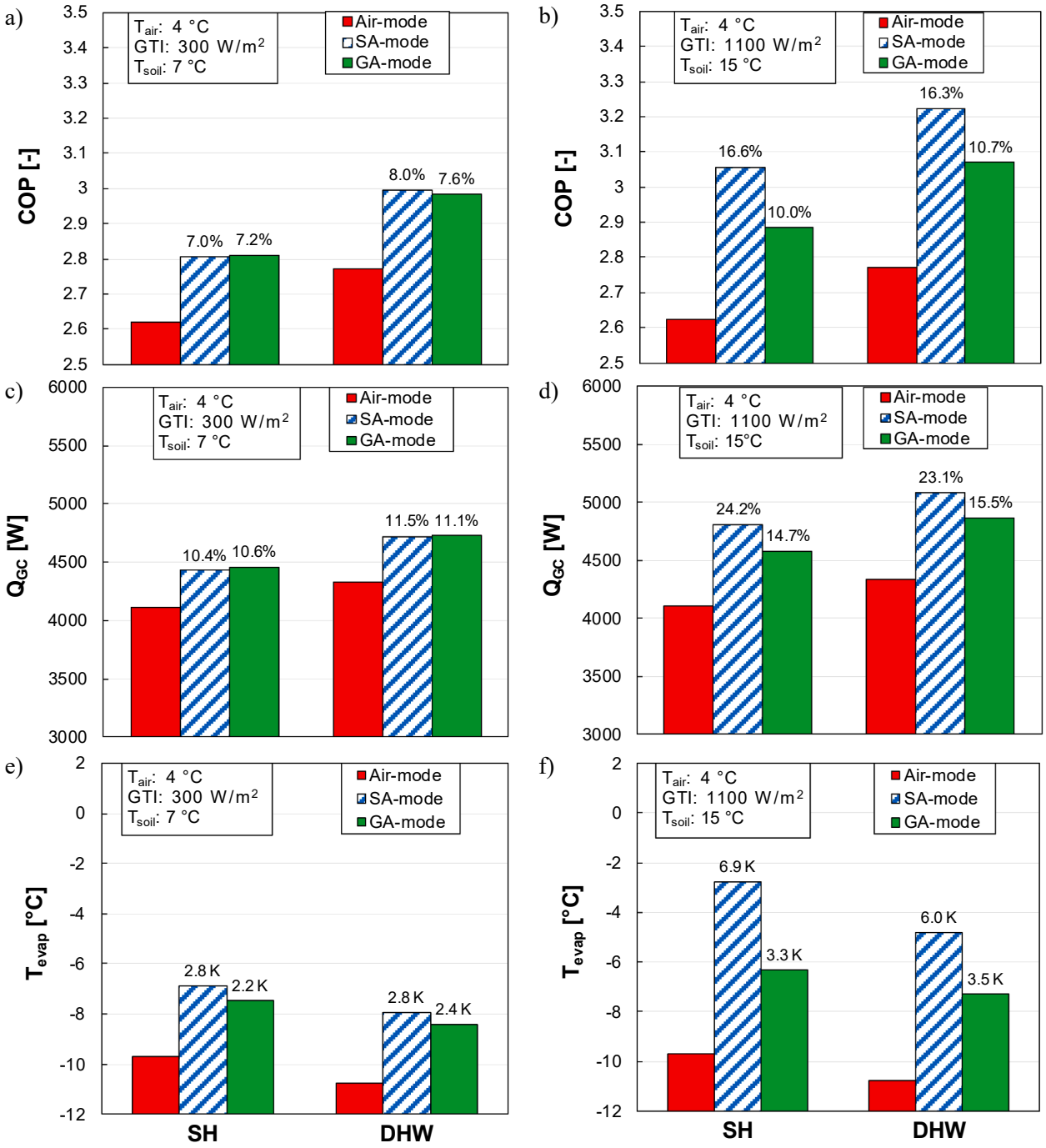

Fig. 13. Comparison between air-mode, SA-mode, and GA-mode for space heating (SH) and domestic hot water (DHW) application, in terms of COP (a,b), heating capacity (c,d), and evaporating temperature (e,f), with various values of GTI and T_{soil}, while T_{air} is fixed at 4 °C. The absolute increase in T_{evap} and the percentage increase in COP and Q_{GC} are reported with respect to the air-mode.

When the contribution of solar and ground sources is low (Fig. 13a), the performances of the SA-mode and the GA-mode are similar, with the COP equal to 2.80 for SH and 2.99 for DHW. Notably, dual-source operation outperforms the air-mode for both applications, achieving approximately a 7 % increase in COP, showing that even a low contribution of solar and ground sources enhances the system performance. When increasing the solar irradiance and the soil temperature, the contribution of solar and ground sources is higher (Fig. 13b) and the COP increases compared to the previous case. In particular, the GA-mode achieves COP values of 2.88 for SH and 3.07 for DHW, while the SA-mode outperforms GA-mode by about 6 % for SH and 5 % for DHW. Notably, the multisource modes always outperform the air-mode for both applications, with the GA-mode and SA-mode achieving 10 % and 16 % increases in COP, respectively. The results show that, as the water temperature difference at the gas cooler increases (which corresponds also to lower values of inlet water temperature at the gas-cooler), the COP of the system increases. This can be attributed to the increase in the heat flow rate at the gas cooler, as shown in Fig. 13b and Fig. 13c. Comparing the results of the heat pump during dual-source operation to those obtained in air-mode, when passing from lower to higher contributions of solar and ground sources, the heat extracted at the gas cooler in SA-mode increases from 10 % to about 23.5 % for both applications, whereas the increase in GA-mode is lower, from about 10 % to about 15 %. A similar trend can be observed for the evaporation temperature. Fig. 13e shows that, when the contribution of the solar and ground sources is low, the evaporation temperature in GA-mode and SA-mode increases by about 2.3 K and 2.8 K, respectively, as compared to the air-mode. For higher GTI and T_{soil} values (Fig. 13f), the increase in evaporation temperature rises to 3.3 K to 6.9 K, respectively, showing the higher contribution of solar and ground sources.

Table 5 summarizes the main results for different applications (SH and DHW) and two cases: a) low contribution of the solar and ground sources, and b) high contribution of solar and ground sources. For SA-mode the total electricity production of the PV cells, which are cooled down by the refrigerant, is around 130 W for case (a) and 900 W for case (b), improving the power production up to 8 % compared to PV cells without cooling. The power extracted at the gas cooler (Q_{GC}) of the multisource heat pump in both operating modes is in the range 4.5–5 kW, with the highest COP equal to 3.22 for DHW production when operating in SA-mode. The results of the present model in GA-mode align with the experimental findings of Bastani et al. [44].

5.3. Effect of the number of boreholes and PV-T modules

The numerical model of the multisource heat pump is here used to investigate the effect of varying the number of BHE (from 1 to 3) in GA-mode and PV-T collectors (from 1 to 4) in SA-mode on the COP of the system (Fig. 14). Varying the number of PV-T modules or boreholes will result in a variation of the evaporation area, significantly affecting the entire evaporation process. The details of the single BHE are listed in Table 1, while those of a single PV-T collector are reported in Sec. 3.4. For comparison, the results of the heat pump operating in air-mode are depicted in the column air-mode. The simulations were performed at two different values of GTI (300 and 1100 W/m^2) and T_{soil} (7 and 13 °C) while maintaining constant the other operating conditions: maximum compressor speed, fan speed set at 50 %, high-pressure maintained at 85 bar, water heated from 30 °C to 40 °C, the refrigerant mass flow rate inside the solar or geothermal evaporators equal to half of the mass flow rate processed by the compressor, and air temperature equal to 4 °C.

Fig. 14a illustrates the effect of the number of PV-T collectors on the COP and heat extracted at the gas cooler (Q_{GC}) during SA-mode (Fig. 14a) at two different GTI values, while the effect of BHE number during GA-mode for two soil temperatures is shown in Fig. 14b. When considering the heat pump working only with the air source, the COP of the heat pump is equal to 2.62. In GA-mode, an increase in the number of BHEs leads to an increase in the COP and Q_{GC}, regardless of the soil temperature T_{soil}. In particular, when passing from 1 to 3 BHEs, the COP increases from 2.81 to 3.01 at T_{soil} equal to 7 °C (7 % increase of COP), while the COP rises from 2.86 to 3.17 at T_{soil} of 13 °C (11 % increase of COP). A similar trend can be observed for the heat extracted at the gas cooler, when passing from 1 to 3 BHEs, Q_{GC} increases from 4460 W to 4780 W at T_{soil} equal to 7 °C, and from 4550 W to 5000 W at T_{soil} of 13 °C.

For the heat pump in SA-mode, when increasing the number of PV-T collectors it results in an increase of COP and Q_{GC} at both GTI of 300 W/m^2 and 1100 W/m^2. In particular, when passing from 1 to 4 PV-T collectors, the COP increases from 2.69 to 2.85 at GTI equal to 300 W/m^2 (6 % increase of COP), while the COP rises from 2.77 to 3.15 at GTI of 1100 W/m^2 (14 % increase of COP). Similarly, Q_{GC} in SA-mode follows the same COP trend, when passing from 1 to 4 PV-T collectors, Q_{GC} increases from 4230 W to 4510 W at GTI equal to 300 W/m^2 and rises from 4370 W to 4940 W at GTI of 1100 W/m^2. Overall, the results indicate that the effect of increasing the number of PV-T panels or BHEs becomes more pronounced with higher GTI or T_{soil}.

It is interesting to note that, compared to the case with zero BHE or PV-T (air-mode), the COP of the multisource heat pump in both SA-mode and GA-mode is higher, even when considering only one PV-T collector or BHE. When considering the GA-mode with one BHE and T_{soil} between 7 °C to 13 °C, an average improvement of 8 % is observed compared to Air-mode. When the number of BHE is equal to 3, the COP increases from 15 % to 21 % respectively with T_{soil} equal to 7 °C and 13 °C compared to air-mode. For the SA-mode with one PV-T collector and GTI ranging between 300 W/m^2 and 1100 W/m^2, an average COP rise of 4 % is achieved. In the case of SA-mode, considering the range of GTI from 300 to 1100 W/m^2, an increase from 8 to 22 % is achieved when the number of PV-Ts is equal to 4. These findings demonstrate the flexibility of the developed multisource heat pump system. Indeed, enhanced

Table 5
Results of the comparison between dual-source operation (SA-mode and GA-mode) with the Air-mode, for SH and DHW applications.

Heat source	Application	Mode	T_{evap} [°C]	Q_{EVAP} [W]	P_{tot} [W]	Q_{GC} [W]	COP [-]
Case a)	SH (30–40 °C)	Air-mode	−9.7	2902	1568	4112	2.62
		SA-mode	−6.9	3205	1578	4427	2.80
		GA-mode	−7.5	3210	1587	4460	2.81
	DHW (20–50 °C)	Air-mode	−10.8	3184	1564	4335	2.77
		SA-mode	−7.9	3551	1577	4722	2.99
		GA-mode	−8.4	3538	1585	4726	2.98
Case b)	SH (30–40 °C)	Air-mode	−9.7	2902	1568	4112	2.62
		SA-mode	−2.8	3605	1573	4811	3.06
		GA-mode	−6.3	3329	1588	4581	2.88
	DHW (20–50 °C)	Air-mode	−10.8	3184	1564	4335	2.77
		SA-mode	−4.8	3921	1579	5089	3.22
		GA-mode	−7.3	3678	1587	4872	3.07

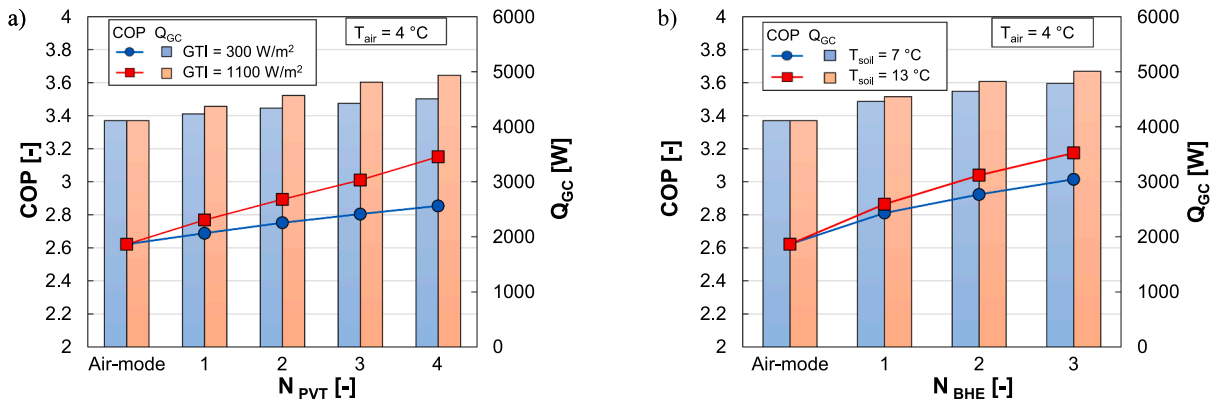

Fig. 14. COP and Q_{GC} values for the SA-mode and GA-mode when the air temperature is equal to 4 °C. Effect of: a) the number of PV-T collectors in SA-mode for two GTI values (300 and 1100 W/m^2) and b) the number of boreholes in GA-mode for two T_{soil} values (7 °C and 13 °C).

performance compared to a standard air-source operation (air-mode) is achieved even when utilizing a limited PV-T evaporator area or a single shallow borehole heat exchanger.

6. Conclusions

The present work numerically investigated the performance of a multisource CO_2 heat pump prototype that can operate in two different modes to exploit air, solar, and ground as low temperature heat sources. In solar-air mode (SA-mode), CO_2 evaporates in both the finned coil heat exchanger and PV-T collectors. In ground-air mode (GA-mode), evaporation occurs in the finned coil and BHE evaporators. In both operating modes, the two evaporators are used simultaneously in direct expansion mode. The performance of the multisource heat pump was evaluated under varying thermal loads and environmental conditions, also in comparison with a reference system operating as an air-source heat pump (air-mode). The key findings of the study are as follows:

- A thermal resistance and capacity numerical model of the borehole heat exchanger was developed and validated to accurately simulate the behavior of the evaporating CO_2 within the BHEs during the GA-mode operation. For the reference climate of Padova, Northern Italy, a shallow 35 m BHE was determined to match the evaporating and heating capacity of the SA-mode under similar operating conditions.
- Performance maps highlight the distinct characteristics of the multisource heat pump in SA-mode and GA-mode under varying environmental conditions. In both systems, the solar or ground evaporators operate simultaneously with the air evaporator and 1 K of air temperature increase results in a 4.8 % COP rise in SA-mode and a 4.3 % COP rise in GA-mode. SA-mode is influenced by solar irradiance, where each 100 W/m^2 GTI increase improves the COP by 2.8 %, while GA-mode is affected by soil temperature and 1 K of T_{soil} increase produce a raise in COP equal to 0.9 %.
- Evaporating temperature (T_{evap}) trends align with COP behavior, with greater sensitivity to T_{air} than GTI or T_{soil}. When increasing GTI or T_{soil} enhances the contribution of PV-T or BHE; however, with the present design conditions, the BHE contribution never dominates for the GA-mode, while PV-T contributions in SA-mode may surpass those of the finned coil at higher GTI. The evaporating temperature of SA-mode increases with both T_{air} and GTI, rising by 0.79 K per 1 K of T_{air} increase and by 0.46 K per 100 W/m^2 of GTI increase. Similarly, in GA-mode, T_{evap} increases almost linearly with T_{air} and T_{soil}, with a stronger influence from T_{air}, where a 1 K rise increases T_{soil} by 0.70 K, while a 1 K of T_{soil} rise increases it by 0.14 K.
- The inlet water temperature at the gas cooler significantly influences the overall COP of the CO_2 multisource heat pump. Two applications of space heating (with the inlet water temperature at the gas cooler equal to 30 °C and exiting at 40 °C) and domestic hot water (with the inlet water temperature at the gas cooler equal to 20 °C and exiting at 50 °C). Whether having a high contribution of GTI or T_{soil}, the COP of the system is always higher for DHW production than SH. More importantly, the COP of the multisource heat pump is always higher than that of the air-source heat pump (air-mode). The increase is equal to 7 % when the contribution of the solar and ground sources is low (GTI = 300 W/m^2 and T_{soil} = 7 °C) and equal to 10 % in GA-mode and 16 % in SA-mode when T_{soil} is equal to 15 °C and GTI is equal to 1100 W/m^2.
- Increasing the number of BHEs or PV-T panels improves the COP compared to the air-source heat pump (air-mode) by enhancing the evaporation process. For GA-mode, adding one to three BHEs results in a 8–21 % COP increase with respect to air-mode within a soil temperature range of 7 °C to 13 °C. For SA-mode, adding one to four PV-Ts achieves a 4–22 % COP increase within a GTI range of 300–1100 W/m^2 compared to air-mode operations. The simultaneous use of the thermal sources allows to consistently outperform the air-mode baseline, with performance gains even with minimal additions of BHEs or PV-Ts, increasing the utilization of renewable energy sources.

Declaration of competing interest

The authors declare the following financial interests/personal relationships which may be considered as potential competing interests: [Financial support by the European Commission - Next Generation EU, Missione 4, Componente C2 Investimento 1.1 “Fondo per il Programma Nazionale di Ricerca e Progetti di Rilevante Interesse Nazionale (PRIN 2022 PNRR)”, CUP C53D23008240001, “Next generation inverse cycles using CO2 based mixtures as refrigerant (CO2MIX)”, project code: P2022C494T].

Acknowledgements

Financial support by the European Commission - Next Generation EU, Missione 4, Componente C2 Investimento 1.1 “Fondo per il Programma Nazionale di Ricerca e Progetti di Rilevante Interesse Nazionale (PRIN 2022 PNRR)”, CUP C53D23008240001, “Next generation inverse cycles using CO2 based mixtures as refrigerant (CO2MIX)”, project code: P2022C494T.

Appendix

The compressor model is composed of three polynomial equations for the calculation of the refrigerant mass flow rate ($\dot{m}_r$), the compressor power consumption (P_{COMP}) and the specific compressor work (Δh_{COMP}). The equations depend on three variables of three degrees, depending on the evaporating temperature (T_{evap}), the pressure at the gas cooler (p_{GC}) and the compressor speed (V_{COMP}). The correlations have been developed from data collected on the prototype explained in Sec. 3.4 during the steady-state operations in the previous study. The polynomial equations have the following form:

$$Y = C_1 \cdot V_{COMP} + C_2 V_{COMP}^2 + C_3 \cdot p_{GC} + C_4 \cdot p_{GC} \cdot V_{COMP} + C_5 \cdot p_{GC} \cdot V_{COMP}^2 + C_6 \cdot {p_{GC}}^2 + C_7 \cdot {p_{GC}}^2 \cdot V_{COMP} + C_8 \cdot T_{evap} + C_9 \cdot T_{evap} \cdot V_{COMP} + C_{10} \cdot T_{evap} \cdot V_{COMP}^2 + C_{11} \cdot T_{evap} \cdot p_{GC} + C_{12} \cdot T_{evap} \cdot p_{GC} \cdot V_{COMP} + C_{13} \cdot T_{evap} \cdot {p_{GC}}^2 + C_{14} \cdot T_{evap}^2 + C_{15} \cdot T_{evap}^2 \cdot V_{COMP} + C_{16} \cdot T_{evap}^2 \cdot p_{GC} + C_{17} + C_{18} \cdot T_{evap}^3 + C_{19} \cdot {p_{GC}}^3 + C_{20} \cdot V_{COMP}^3$$

The 20 experimental coefficients are reported in Table A.

Table A
Polynomial coefficients of the compressor.

Coefficient	$\dot{m}_r$ [kg/s]	P_{COMP} [W]	Δh_{COMP} [J/kg]
C_1	2.138E-04	15.875	1399.536
C_2	4.008E-06	−0.00203	−11.784
C_3	6.017E-03	−155.281	18801.46
C_4	5.088E-06	−0.202	−7.807
C_5	2.489E-08	0.000579	−0.00559
C_6	7.957E-05	2.141	−215.654
C_7	5.058E-08	0.00156	0.047
C_8	−5.733E-03	−41.538	3622.331
C_9	2.860E-05	0.151	−70.687
C_{10}	−1.612E-07	−0.00483	0.338
C_{11}	1.203E-04	0.672	−46.332
C_{12}	−4.686E-08	0.00528	0.139
C_{13}	−6.713E-07	−0.00501	0.150
C_{14}	3.870E-05	0.754	−78.484
C_{15}	6.321E-07	−0.0125	0.986
C_{16}	1.953E-08	−0.00339	0.162
C_{17}	1.528E-01	3554.001	−548464
C_{18}	−5.997E-07	−0.0137	−1.310
C_{19}	−3.514E-07	−0.00934	0.850
C_{20}	−1.206E-08	−0.000065	0.0546

Data availability

Data will be made available on request.

References

[1] E.U. Directive 2012/27/EU on Energy Efficiency, amending Directives 2009/12/EC and 2010/30/EU and repealing Directives 2004/8/EC and 2006/32/EC, 25 October 2012., (n.d.).
[2] A. Philippe, L. Jean, EBC Annex 48: Heat pumping and reversible air conditioning-Project summary report, (2016).
[3] F. Wang, R. Zhao, W. Xu, D. Huang, Z. Qu, A heater-assisted air source heat pump air conditioner to improve thermal comfort with frost-retarded heating and heat-uninterrupted defrosting, Energies (Basel) 14 (2021) 2646.
[4] Z. Li, W. Wang, Y. Sun, S. Wang, S. Deng, Y. Lin, Applying image recognition to frost built-up detection in air source heat pumps, Energy 233 (2021) 121004.
[5] Y. Guo, G. Zhang, J. Zhou, J. Wu, W. Shen, A techno-economic comparison of a direct expansion ground-source and a secondary loop ground-coupled heat pump system for cooling in a residential building, Appl. Therm. Eng. 35 (2012) 29–39, https://doi.org/10.1016/j.applthermaleng.2011.09.032.
[6] R.S. Kamel, A.S. Fung, P.R.H. Dash, Solar systems and their integration with heat pumps: a review, Energy Build. 87 (2015) 395–412, https://doi.org/10.1016/j.enbuild.2014.11.030.
[7] H.M. Skye, W. Wu, Experiments and exergy analysis for a carbon dioxide ground-source heat pump in cooling mode, Int. J. Refrig 131 (2021) 920–937, https://doi.org/10.1016/j.ijrefrig.2021.08.018.
[8] A. Hakkaki-Fard, P. Eslami-Nejad, Z. Aidoun, M. Ouzzane, A techno-economic comparison of a direct expansion ground-source and an air-source heat pump system in Canadian cold climates, Energy 87 (2015) 49–59, https://doi.org/10.1016/j.energy.2015.04.093.
[9] J. Choi, B. Kang, H. Cho, Performance comparison between R22 and R744 solar-geothermal hybrid heat pumps according to heat source conditions, Renew. Energy 71 (2014) 414–424, https://doi.org/10.1016/J.RENENE.2014.05.057.
[10] B.T. Austin, K. Sumathy, Parametric study on the performance of a direct-expansion geothermal heat pump using carbon dioxide, Appl. Therm. Eng. 31 (2011) 3774–3782, https://doi.org/10.1016/j.applthermaleng.2011.07.007.
[11] S. Bordignon, G. Emmi, A. Zarrella, M. De Carli, Energy analysis of different configurations for a reversible ground source heat pump using a new flexible TRNSYS Type, Appl. Therm. Eng. 197 (2021) 117413, https://doi.org/10.1016/j.applthermaleng.2021.117413.
[12] S. Faisal Ahmed, M. Khalid, M. Vaka, R. Walvekar, A. Numan, A. Khaliq Rasheed, N. Mujawar Mubarak, Recent progress in solar water heaters and solar collectors: a comprehensive review, Therm. Sci. Eng. Prog. 25 (2021) 100981, https://doi.org/10.1016/j.tsep.2021.100981.
[13] K. Sezen, A. Gungor, Comparison of solar assisted heat pump systems for heating residences: a review, Sol. Energy 249 (2023) 424–445, https://doi.org/10.1016/j.solener.2022.11.051.
[14] E. Zanetti, M. Azzolin, S. Girotto, D. Del Col, Performance and control of a CO_2 dual source solar assisted heat pump with a photovoltaic-thermal evaporator, Appl. Therm. Eng. 218 (2023) 119286, https://doi.org/10.1016/j.applthermaleng.2022.119286.
[15] J. Chen, D. Wang, G. Zhang, X. Peng, X. Qin, G. Wang, 4E analyses of a novel solar-assisted vapor injection autocascade high-temperature heat pump based on genetic algorithm, Energy Convers. Manag. 299 (2024) 117863, https://doi.org/10.1016/J.ENCONMAN.2023.117863.
[16] EU No 2024/573, Regulation (EU) 2024/573 of the European Parliament and of the Council of 7 February 2024 on fluorinated greenhouse gases, amending Directive (EU) 2019/1937 and repealing Regulation (EU) No 517/2014, (n.d.).
[17] A. James, M. Srinivas, M. Mohanraj, A.K. Raj, S. Jayaraj, Experimental studies on photovoltaic-thermal heat pump water heaters using variable frequency drive compressors, Sustain. Energy Technol. Assess. 45 (2021) 101152, https://doi.org/10.1016/j.seta.2021.101152.
[18] G.-H. Shi, L. Aye, D. Li, X.-J. Du, Recent advances in direct expansion solar assisted heat pump systems: a review, Renew. Sustain. Energy Rev. 109 (2019) 349–366, https://doi.org/10.1016/j.rser.2019.04.044.
[19] S.N. Rabelo, T.F. Paulino, W.M. Duarte, A.A.T. Maia, L. Machado, Experimental analysis of the influence of the expansion valve opening on the performance of the

small size CO_2 solar assisted heat pump, Sol. Energy 190 (2019) 255–263, https://doi.org/10.1016/j.solener.2019.08.013.
[20] E. Zanetti, S. Bordignon, R. Conte, A. Bisi, M. Azzolin, A. Zarrella, Experimental and numerical analysis of a CO_2 dual-source heat pump with PVT evaporators for residential heating applications, Appl. Therm. Eng. 233 (2023) 121165, https://doi.org/10.1016/j.applthermaleng.2023.121165.
[21] H. Wang, Q. Zhao, J. Wu, B. Yang, Z. Chen, Experimental investigation on the operation performance of a direct expansion ground source heat pump system for space heating, Energy Build 61 (2013) 349–355, https://doi.org/10.1016/j.enbuild.2013.02.042.
[22] W. Yang, Experimental performance analysis of a direct-expansion ground source heat pump in Xiangtan, China, Energy 59 (2013) 334–339, https://doi.org/10.1016/j.energy.2013.07.036.
[23] M. De Carli, S. Fiorenzato, A. Zarrella, Performance of heat pumps with direct expansion in vertical ground heat exchangers in heating mode, Energy Convers. Manag. 95 (2015) 120–130, https://doi.org/10.1016/j.enconman.2015.01.080.
[24] T.A. Sazon, Q. Zhang, H. Nikpey, Comparison of different configurations of a solar-assisted ground-source CO_2 heat pump system for space and water heating using Taguchi-Grey Relational analysis, Energy Convers. Manag. 300 (2024) 117881, https://doi.org/10.1016/J.ENCONMAN.2023.117881.
[25] F. Pelella, G. Zsembinszki, L. Viscito, A. William Mauro, L.F. Cabeza, Thermo-economic optimization of a multi-source (air/sun/ground) residential heat pump with a water/PCM thermal storage, Appl. Energy 331 (2023) 120398, https://doi.org/10.1016/j.apenergy.2022.120398.
[26] I. Grossi, M. Dongellini, A. Piazzi, G.L. Morini, Dynamic modelling and energy performance analysis of an innovative dual-source heat pump system, Appl. Therm. Eng. 142 (2018) 745–759, https://doi.org/10.1016/j.applthermaleng.2018.07.022.
[27] S. Siren, J. Hirvonen, P. Sormunen, Comparison of traditional and ambient air-assisted ground source heat pump systems using different bore field configurations, Energy Convers. Manag. 323 (2025) 119240, https://doi.org/10.1016/J.ENCONMAN.2024.119240.
[28] K. Balaji, V. Sharma, Energy demand reduction in the built environment using shallow geothermal integrated energy systems: part ii—hybrid ground source heat pump for building heating, ASME J. Eng. Sustain. Build. Cities 2 (2021), https://doi.org/10.1115/1.4052215.
[29] J. Li, S. Wei, Y. Dong, X. Liu, V. Novakovic, Technical and economic performance study on winter heating system of air source heat pump assisted solar evacuated tube water heater, Appl. Therm. Eng. 221 (2023) 119851, https://doi.org/10.1016/j.applthermaleng.2022.119851.
[30] M. Qu, J. Chen, L. Nie, F. Li, Q. Yu, T. Wang, Experimental study on the operating characteristics of a novel photovoltaic/thermal integrated dual-source heat pump water heating system, Appl. Therm. Eng. 94 (2016) 819–826, https://doi.org/10.1016/j.applthermaleng.2015.10.126.
[31] H. Thieblemont, F. Haghighat, R. Ooka, A. Moreau, Predictive control strategies based on weather forecast in buildings with energy storage system: a review of the state-of-the art, Energy Build. 153 (2017) 485–500, https://doi.org/10.1016/j.enbuild.2017.08.010.
[32] Y. Wang, Z. Quan, H. Jing, L. Wang, Y. Zhao, Performance and operation strategy optimization of a new dual-source building energy supply system with heat pumps and energy storage, Energy Convers. Manag. 239 (2021) 114204, https://doi.org/10.1016/j.enconman.2021.114204.
[33] R. Conte, E. Zanetti, M. Tancon, M. Azzolin, S. Girotto, D. Del Col, The advantage of running a direct expansion CO_2 heat pump with solar-and-air simultaneous heat sources: experimental and numerical investigation, Appl. Energy 369 (2024) 123478, https://doi.org/10.1016/j.apenergy.2024.123478.
[34] E.W. Lemmon, M.L. Huber, M.O. McLinden, NIST standard reference database 23, Reference Fluid Thermodynamic and Transport Properties (REFPROP) 9 (2010).
[35] D. Bauer, W. Heidemann, H.-J.-G. Diersch, Transient 3D analysis of borehole heat exchanger modeling, Geothermics 40 (2011) 250–260, https://doi.org/10.1016/j.geothermics.2011.08.001.
[36] L. Cheng, G. Ribatski, J.R. Thome, New prediction methods for CO_2 evaporation inside tubes: part ii—an updated general flow boiling heat transfer model based on flow patterns, Int. J. Heat Mass Transf. 51 (2008) 125–135.
[37] V. Gnielinski, New equations for heat and mass transfer in turbulent pipe and channel flow, Int. Chem. Eng. 16 (1976) 359–367.
[38] M. Badache, M. Ouzzane, P. Eslami-Nejad, Z. Aidoun, Experimental study of a carbon dioxide direct-expansion ground source heat pump (CO_2-DX-GSHP), Appl. Therm. Eng. 130 (2018) 1480–1488, https://doi.org/10.1016/j.applthermaleng.2017.10.159.
[39] E. Zanetti, S. Bonduà, S. Bortolin, V. Bortolotti, M. Azzolin, F. Tinti, Sequential coupled numerical simulations of an air/ground-source heat pump: Validation of the model and results of yearly simulations, Energy Build. 277 (2022) 112540, https://doi.org/10.1016/j.enbuild.2022.112540.
[40] E. Zanetti, M. Azzolin, S. Bortolin, G. Busato, D. Del Col, Experimental data and modelling of a dual source reversible heat pump equipped with a minichannels evaporator, Therm. Sci. Eng. Prog. 35 (2022) 101471, https://doi.org/10.1016/j.tsep.2022.101471.
[41] E. Zanetti, M. Azzolin, R. Conte, S. Girotto, D. Del Col, Experiments and dynamic modelling of dry expansion and flooded evaporators in a CO_2 solar assisted heat pump, Appl. Therm. Eng. 217 (2022) 118964, https://doi.org/10.1016/j.applthermaleng.2022.118964.
[42] ENEA, (n.d.). http://www.solaritaly.enea.it/TabelleRad/TabelleRadIt.php (accessed November 30, 2024).
[43] EnergyPlus, (n.d.). https://energyplus.net/ (accessed November 30, 2024).
[44] A. Bastani, P. Eslami-Nejad, M. Badache, A.T.A. Nguyen, Experimental characterization of a transcritical CO_2 direct expansion ground source heat pump for heating applications, Energy Build. 212 (2020) 109828, https://doi.org/10.1016/j.enbuild.2020.109828.